A Basin- to Channel-Scale Unstructured Grid Hurricane Storm Surge Model Applied to Southern Louisiana

JOANNES J. WESTERINK,* RICHARD A. LUETTICH,+ JESSE C. FEYEN,*,++ JOHN H. ATKINSON,*,## CLINT DAWSON,# HUGH J. ROBERTS,*,@@ MARK D. POWELL,@ JASON P. DUNION,& ETHAN J. KUBATKO,* AND HASAN POURTAHERI**

*Department of Civil Engineering and Geological Sciences, University of Notre Dame, Notre Dame, Indiana
+Institute of Marine Sciences, University of North Carolina at Chapel Hill, Chapel Hill, North Carolina
#Institute for Computational Engineering and Sciences, University of Texas at Austin, Austin, Texas
@Hurricane Research Division, National Oceanic and Atmospheric Administration, Miami, Florida
&University of Miami–NOAA/Cooperative Institute for Marine and Atmospheric Studies, National Oceanic and Atmospheric Administration, Miami, Florida
**U.S. Army Corps of Engineers, New Orleans District, New Orleans, Louisiana

(Manuscript received 7 July 2006, in final form 20 June 2007)

ABSTRACT

Southern Louisiana is characterized by low-lying topography and an extensive network of sounds, bays, marshes, lakes, rivers, and inlets that permit widespread inundation during hurricanes. A basin- to channel-scale implementation of the Advanced Circulation (ADCIRC) unstructured grid hydrodynamic model has been developed that accurately simulates hurricane storm surge, tides, and river flow in this complex region. This is accomplished by defining a domain and computational resolution appropriate for the relevant processes, specifying realistic boundary conditions, and implementing accurate, robust, and highly parallel unstructured grid numerical algorithms.

The model domain incorporates the western North Atlantic, the Gulf of Mexico, and the Caribbean Sea so that interactions between basins and the shelf are explicitly modeled and the boundary condition specification of tidal and hurricane processes can be readily defined at the deep water open boundary. The unstructured grid enables highly refined resolution of the complex overland region for modeling localized scales of flow while minimizing computational cost. Kinematic data assimilative or validated dynamic-modeled wind fields provide the hurricane wind and pressure field forcing. Wind fields are modified to incorporate directional boundary layer changes due to overland increases in surface roughness, reduction in effective land roughness due to inundation, and sheltering due to forested canopies. Validation of the model is achieved through hindcasts of Hurricanes Betsy and Andrew. A model skill assessment indicates that the computed peak storm surge height has a mean absolute error of 0.30 m.

1. Introduction

The geography of southern Louisiana is defined by a low-lying coastal floodplain situated adjacent to a broad continental shelf. A large delta has been formed by the Mississippi River that extends nearly to the continental shelf break. The region is covered by interconnected sounds, bays, marshes, lakes, rivers, inlets, and channels, while the major relief is defined by features such as barrier islands, salt domes, river banks, and an extensive system of levees and raised roads and railroads. The region is changing significantly in time due to natural morphological evolution, man-made levees, and other processes that have led to a sediment-starved delta that is slowly subsiding (Coleman et al. 1998). The low-lying topography, the ubiquitous water bodies, and the intricate system of raised features make the region very susceptible to flooding from hurricane storm surge. Hurricane surges can propagate rapidly across

++ Current affiliation: Coast Survey Development Laboratory, National Oceanic and Atmospheric Administration, Silver Spring, Maryland.
Current affiliation: Ayres Associates, Fort Collins, Colorado.
@@ Current affiliation: Arcadis U.S., Denver, Colorado.

Corresponding author address: Joannes Westerink, Dept. of Civil Engineering and Geological Sciences, University of Notre Dame, 156 Fitzpatrick Hall, Notre Dame, IN 46556.
E-mail: jjw@photius.ce.nd.edu

DOI: 10.1175/2007MWR1946.1

the floodplain from many directions and can develop dramatic localized amplification due to the topography and raised features. This geometrically and hydrodynamically complex region is one of the most challenging areas in the world to correctly model hurricane-induced flooding.

Coastal flooding is driven by wind, atmospheric pressure gradients, tides, river flow, short-crested wind waves, and rainfall. A numerical model of coastal inundation requires an accurate description of the geographic system, process dynamics, forcing mechanisms, and far-field boundary conditions. These issues are closely related and depend upon domain selection, model physics, the computational resolution of local-scale geography and energetic flow processes, numerical algorithms, and the speed of the software and hardware.

We have developed an unstructured-grid finite-element hydrodynamic model to simulate coupled storm surge, tides, and riverine flow in southern Louisiana. We emphasize an accurate description of the region's topography, bathymetry, predominant physical features, and flow dynamics. The model incorporates a basin-scale domain that simplifies specification of the open-ocean boundary condition for both tides and storm surge (Blain et al. 1994; Westerink et al. 1994a), while providing high resolution within regions of rapidly varying geometry and flow response. Application of unstructured grids to resolve the energetic scales of motion on a localized basis enables an accurate solution of the governing equations while minimizing the number of computational nodes. Tides and surge waves can typically be coarsely resolved in deep waters while requiring finer resolution on the shelf (Luettich and Westerink 1995; Blain et al. 1998). Furthermore, it is clear that resolution of critical small-scale features such as inlets, rivers, and navigation channels is necessary in the coastal floodplain.

The physical processes in the hydrodynamic model are described by the depth-averaged shallow-water equations (SWE). These equations are widely used to describe coupled storm surge, tides, and riverine flows in the coastal ocean and adjacent floodplain. Processes that exist at the physical boundaries of the water column and on the subgrid scale are parameterized; these include bottom shear stress, momentum diffusion, free-surface shear stress due to winds, and subgrid-scale obstructions such as levees. Meteorological forcing is optimized through application of either data-assimilated wind fields or validated wind models. Modification of hurricane wind fields by land roughness has been included by quantifying the wind boundary layer adjustment through an upwind directional land roughness parameterization, by adjusting land roughness according to the depth of local inundation, and by accounting for the existence of heavily forested canopies.

To validate the model, we have hindcast Hurricanes Betsy (1965) and Andrew (1992). These were well documented, powerful storms that resulted in widespread flooding in southeastern Louisiana. We did not perform any model tuning by adjusting model parameters but did implement selective intrasimulation grid refinement and improvements in the definition of the topography, bathymetry, raised features, and channels in order to improve the quality of the hindcasts. All subgrid-scale processes, including bottom friction coefficient, air–sea momentum transfer, and levee weir coefficients, were selected based on standard values that are widely used in engineering practice and literature. While geographic and grid refinement improve the quality of the solution, they do not constitute model tuning since this refinement process more accurately defines the existing physical system and flow fields and is an ordered converging process. An assessment was made of the model's skill by comparing measured and computed hydrographs and high-water marks.

2. Domain definition and unstructured grid development

Our southern Louisiana storm surge model domain includes the western North Atlantic, the Gulf of Mexico, and the Caribbean Sea. The domain (Fig. 1) has a geometrically simple and primarily deep-water open-ocean boundary that lies along the 60°W meridian (Westerink et al. 1994a; Blain et al. 1994; Mukai et al. 2002). The tidal response on this boundary is dominated by the astronomical constituents, nonlinear energy is limited due to the large depth, and the boundary is not located in a resonant basin or near tidal amphidromes. Hurricane storm surge response along this boundary is essentially an inverted barometer pressure effect computed using the atmospheric pressure deficit; it can therefore be easily specified. This boundary allows the model to accurately capture basin-to-basin and basin-to-shelf physics associated with tide- and hurricane-driven events.

Much of the domain is bordered by a land boundary made up of the eastern coastlines of North, Central, and South America. In southern Louisiana the domain includes a large overland region (Figs. 1–3; see also Table 1). The land boundary extends inland and runs along major hydraulic controls including Interstate 10 and U.S. Route 190 in the western part of the state, the entire Atchafalaya flood basin to Simmesport in the

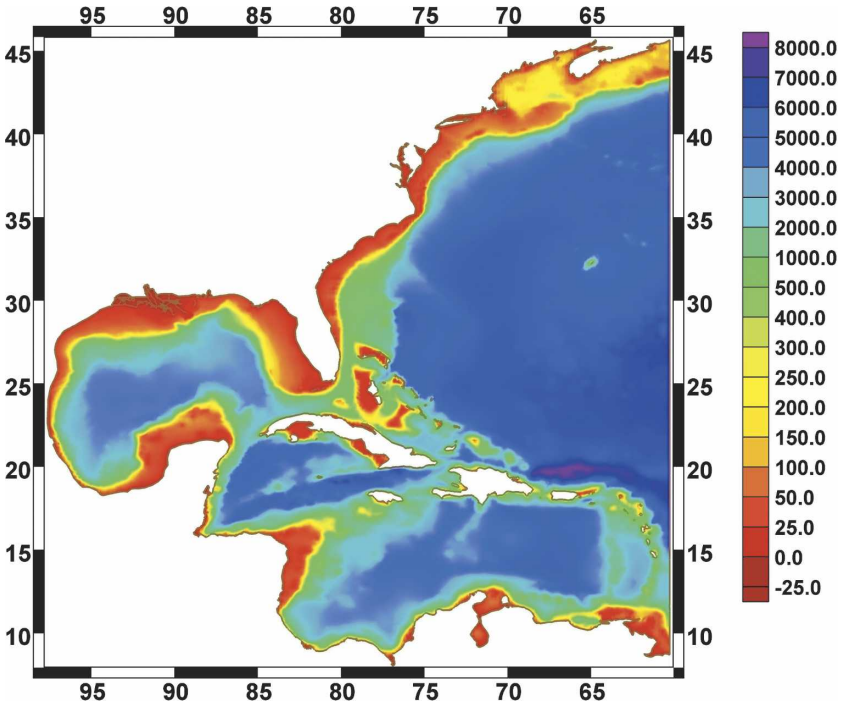

FIG. 1. Western North Atlantic, Gulf of Mexico, and Caribbean Sea computational domain with bathymetry (m).

central part of the state, and Interstates 12/10 north of Lake Pontchartrain in the eastern part of the state.

The domain includes critical hydraulic features and controls that both enhance and attenuate storm surge. We have incorporated the Mississippi River up to Baton Rouge and the Atchafalaya River up to Simmesport since both locations have available reliable water surface elevation gauge data and have adjacent to-

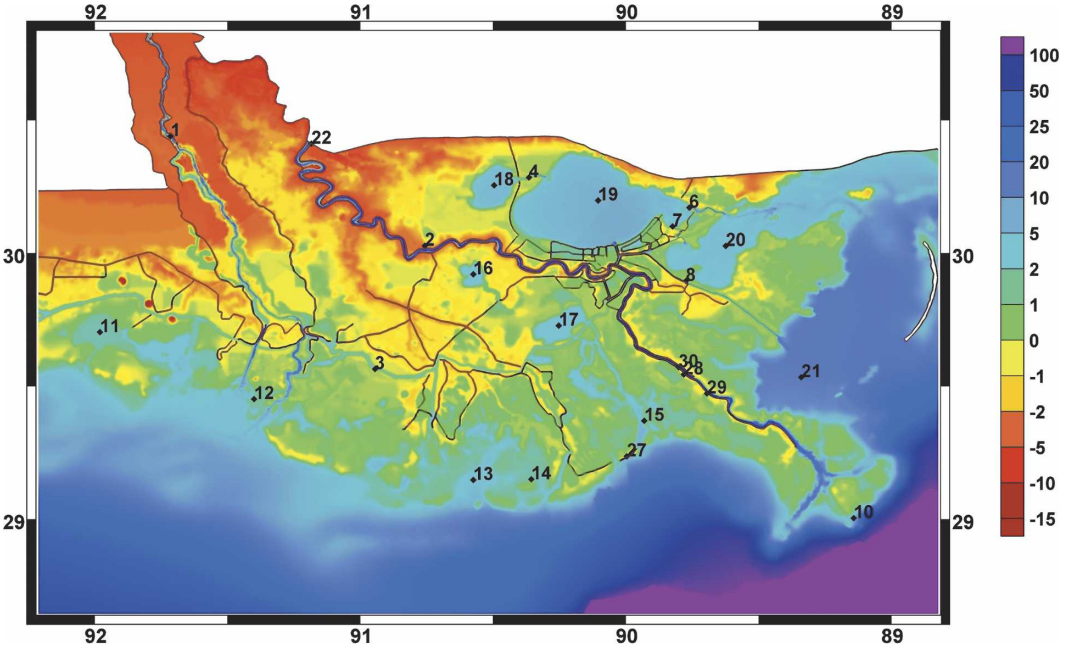

FIG. 2. Detail of bathymetry and topography (m) across southeastern LA, with raised features shown in brown. Geographic locations of interest are indicated by numbers identified in Table 1.

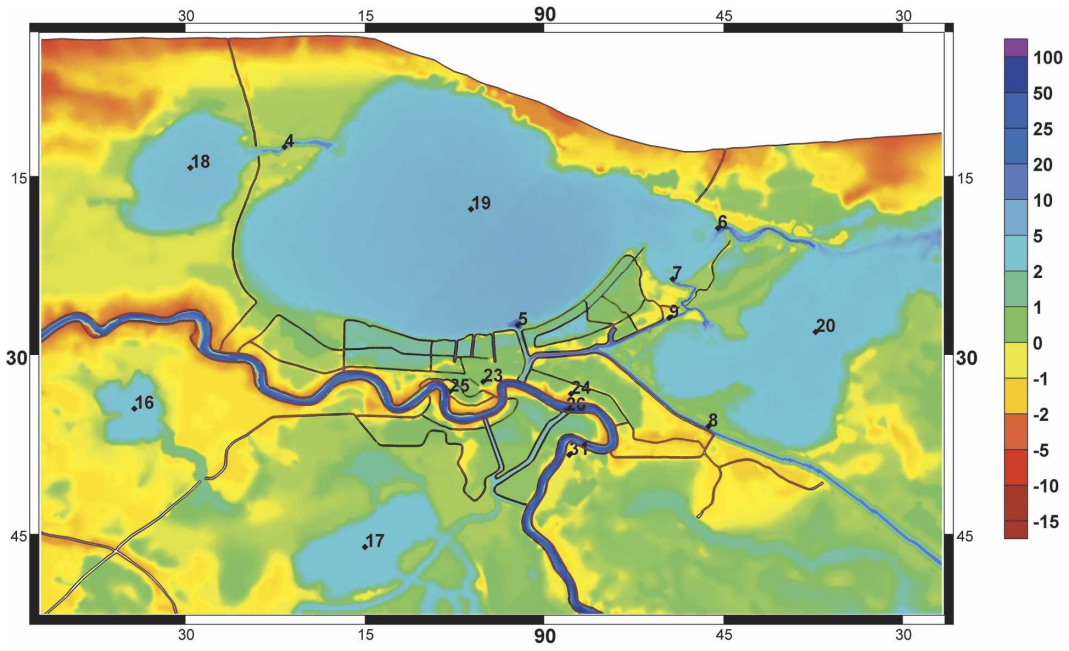

FIG. 3. Detail of bathymetry and topography (m) across metropolitan New Orleans and Lake Pontchartrain, with raised features shown in brown. Geographic locations of interest are indicated by numbers identified in Table 1.

pography that is not susceptible to hurricane inundation. In addition, major dredged navigation canals including the Gulf Intracoastal Waterway (GIWW), the Inner Harbor Navigation Canal (IHNC), the Mississippi River Gulf Outlet (MRGO), Chef Menteur Pass, the Rigolets, and lakes and bays including Lake Pontchartrain, Lake Maurepas, Lake Borgne, Barataria Bay, Timbalier Bay, Terrebonne Bay, Vermillion Bay, Calcasieu Lake and Sabine Lake are represented. We note that the interconnectivity between the various water bodies significantly impacts water levels throughout the system. For example, the Rigolets and Chef Menteur Pass, connecting Lake Borgne and Lake Pontchartrain, as well as Pass Manchac, connecting Lake Pontchartrain and Lake Maurepas, provide significant hydraulic connectivity between these lakes and tend to lower water levels in the lakes to the east while raising water levels in the lakes to the west.

The federal levee system, interstate and state highways, and railroads that are elevated above the surrounding topography and that are not on piles act as hydraulic controls and have been included as weirs. The levee and raised topographic systems surround many rivers, lakes, and cities including the Mississippi River, the western shore of Lake Pontchartrain, the city of New Orleans and the channels that intersect it, as well as the area around the Atchafalaya flood basin. Federal levees and roads are defined with crown heights as they existed in 1965 for the Hurricane Betsy hindcast and as they existed in 2002 for the Hurricane Andrew hindcast. We note that the levees around St. Bernard and New Orleans East in particular were either built or substantially raised after Hurricane Betsy in 1965. We note that the Mississippi River levees tend to hydraulically isolate the east and west banks for all but the largest storms. However, the configuration of the river levees does allow for large surges to develop and propagate up river. Furthermore, flood controls such as the Bonne Carre Spillway can affect the connectivity between the river and Lake Pontchartrain, although for the low-river stages that occurred during the storms we examined, this structure was kept closed.

Bathymetric and topographic data were obtained from a variety of sources. The 5′ Gridded Earth Topography (ETOPO5) database was used to provide bathymetric values in deep water as well as in non-U.S. areas (National Geophysical Data Center 2006). In U.S. continental shelf waters, the National Oceanic and Atmospheric Administration (NOAA) depth sounding database was used (National Geophysical Data Center 1998). Within southern Louisiana, U.S. Geological Survey (USGS) topographic survey values were applied (U.S. Geological Survey 2006). The depths of navigable rivers and channels were obtained from the U.S. Army Corps of Engineers New Orleans District (USACE-MVN) and dredging contractor surveys. An element-based gathering–averaging procedure that sums and averages all surface elevation data located within a cluster

TABLE 1. Geographic location by type and number shown in Figs. 2 and 3.

	Rivers and channels
1	Atchafalaya River
2	Mississippi River
3	GIWW-west
4	Pass Manchac
5	IHNC
6	Rigolets
7	Chef Menteur Pass
8	MRGO
9	GIWW-east
10	South Pass
	Bays, lakes, and sounds
11	Vermilion Bay
12	Atchafalaya Bay
13	Terrebonne Bay
14	Timbalier Bay
15	Barataria Bay
16	Lac Des Allemands
17	Lake Salvador
18	Lake Maurepas
19	Lake Pontchartrain
20	Lake Borgne
21	Breton Sound
	Places
22	Baton Rouge
23	New Orleans
24	Chalmette
25	Carrollton
26	Algiers Lock
27	Grand Isle
28	Diamond
29	Port Sulphur
30	Pointe a la Hache
31	English Turn

of finite elements surrounding a given node was used to interpolate these data onto our unstructured grid, which essentially implements grid-scale filtering and ensures that the bathymetry and topography are consistent with the scale of the grid. It is noted that the bathymetry and topography were defined to best represent the present-day system although some of the National Ocean Service (NOS) bathymetric data in particular may have been collected as much as decades earlier.

It is necessary to reference the vertical datums used for the bathymetric and topographic data to the model's vertical datum. Bathymetry is referenced to the tidal mean lower low water (MLLW). NOAA benchmarks in southern Louisiana indicate that local mean sea level (LMSL) is on average 18 cm above MLLW datum. Similarly, USGS topographic data are referenced to the National Geodetic Vertical Datum of 1929 (NGVD29); at tidal benchmark locations in Louisiana,

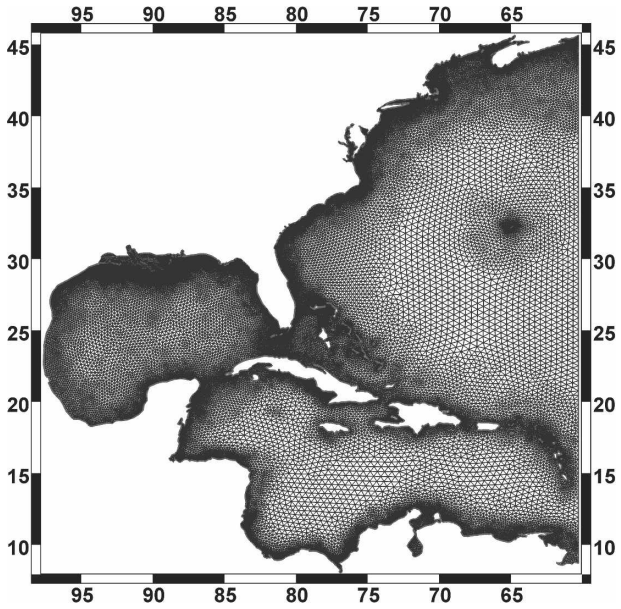

FIG. 4. Unstructured S08 grid of the entire domain.

LMSL is above NGVD29 by 10 cm or more. We neglect the 8-cm difference between MLLW and NGVD29 and raise the initial water height by 18 cm so that the model vertical datum matches NGVD29 on a regional average basis. We note that spatial variability in this rapidly subsiding region will create local differences from this offset. In fact, subsidence rates in the delta have been determined to be as high as 10–15 mm yr^{-1} (Shinkle and Dokka 2004).

The computational grid, shown in Figs. 4–6, consists of linear triangular finite elements whose vertices are connected by nodes at which surface water elevations and velocities are computed. The size of the finite elements in meters is shown in Figs. 7–9. This grid has been constructed to provide sufficient resolution for the tidal, wind, atmospheric pressure, and riverine flow forcing functions from the ocean basins to the coastal floodplain. Efficient and accurate resolution of tides within the basins and on the shelf is determined by tidal wavelength criteria and topographic length-scale criteria (Westerink et al. 1994a; Luettich and Westerink 1995; Hagen et al. 2000, 2001). Hurricane forcing and response are also considered when determining the level of resolution required in order to accurately model hurricane effects. In deep water, underresolution of the inverted barometer forcing function results in underprediction of the peak inverted barometer effect. In shallow water, underresolution of the grid can lead to a significant overprediction of peak storm surge, and therefore enhanced resolution in shelf waters adjacent to hurricane landfall locations is critical (Blain et al. 1998).

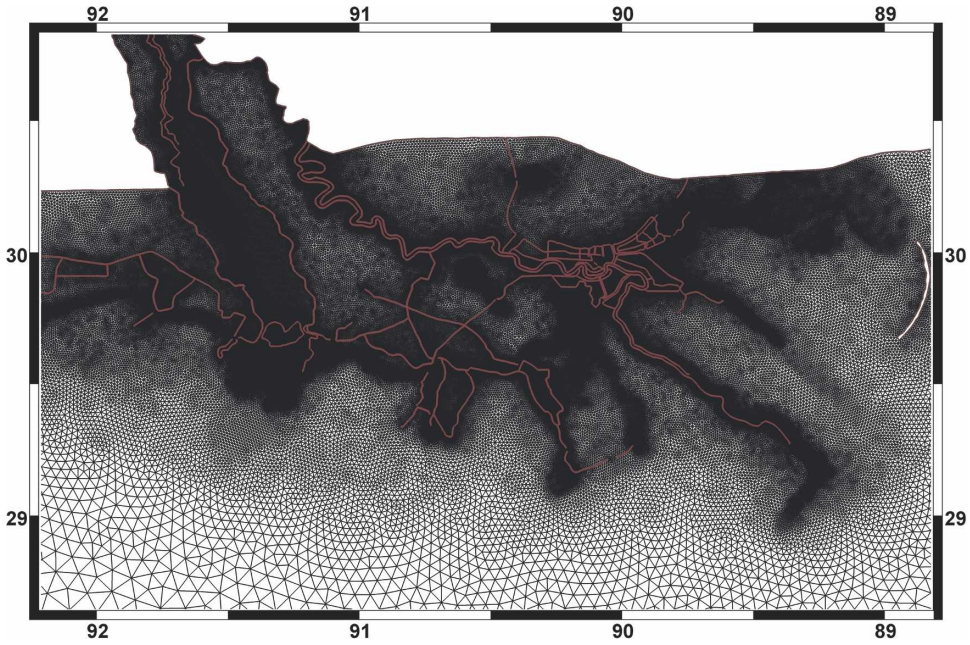

FIG. 5. Detail of the unstructured S08 grid in southeastern LA with raised features shown in brown.

The grid design provides localized refinement of the southern Louisiana coastal floodplain and its hydraulic features. The overland regions and lakes in southern Louisiana are typically resolved at about 500 m, but most waterways and structures controlling surge propagation have a much finer resolution. Grid sensitivity studies in rivers and in the Lake Pontchartrain–Lake Borgne system have indicated that underresolution significantly reduces conveyance and therefore dampens tides, riverine flows, and surge propagation into rivers

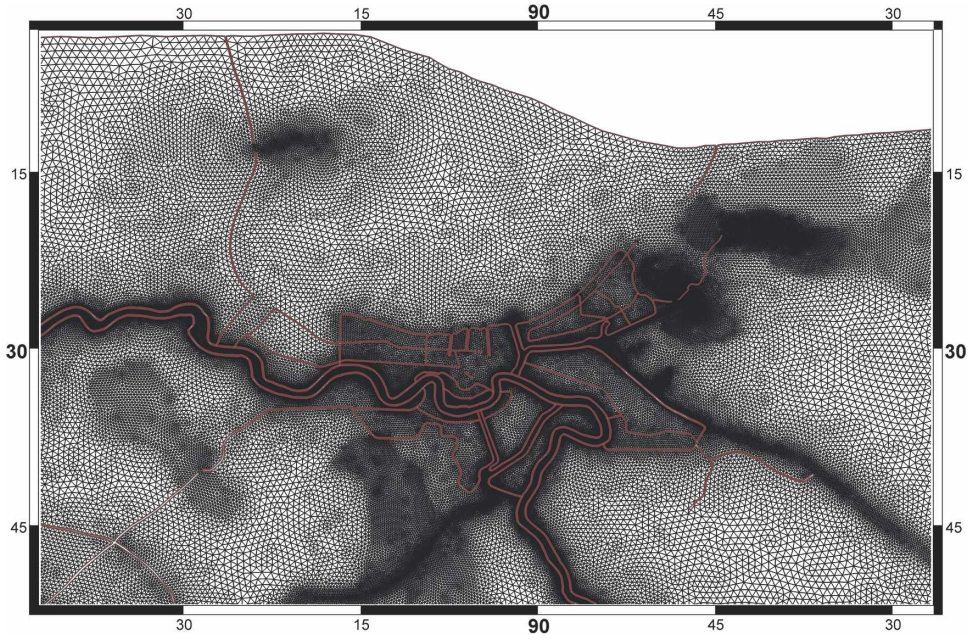

FIG. 6. Detail of the unstructured S08 grid across metropolitan New Orleans and Lake Pontchartrain, with raised features shown in brown.

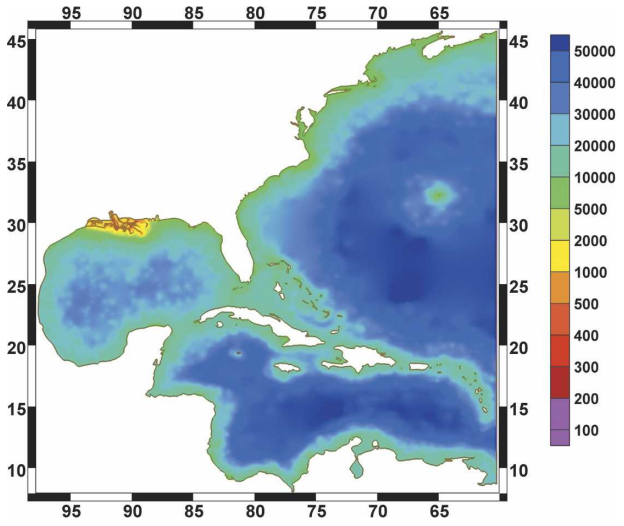

FIG. 7. Finite-element sizes for the S08 grid in m.

and inlets (Feyen et al. 2002). Therefore, the grid generally applies five or more nodes across the major rivers and inlets with grid sizes of 100–200 m.

The wide range of element sizes demonstrates the significant advantages of an unstructured grid: resolution is governed by local flow scales, and the computational cost is minimized. The unstructured grid used in this work is designated as the S08 grid and contains 314 442 nodes and 600 331 elements. Grid resolution varies from approximately 50 km in the deep Atlantic Ocean to less than 100 m in channels. The high resolution required for the study region leads to a final grid with more than 85% of the computational nodes placed within or on the shelf adjacent to southern Louisiana. Therefore, use of a large-scale domain adds only 15% to the computational cost of the simulations.

3. ADCIRC hydrodynamic model

a. Governing equations

The two-dimensional, depth-integrated implementation of the Advanced Circulation (ADCIRC-2DDI) coastal ocean model was used to perform the hydrodynamic computations in this study (Luettich et al. 1992; Kolar et al. 1994a; Luettich and Westerink 2006b). The governing shallow-water equations (SWEs) in primitive, nonconservative, and barotropic form in spherical coordinates are given by

$$\frac{\partial \zeta}{\partial t} + \frac{1}{R\cos\phi}\left(\frac{\partial UH}{\partial \lambda} + \frac{\partial (VH\cos\phi)}{\partial \phi}\right) = 0, \tag{1}$$

$$\frac{\partial U}{\partial t} + \frac{1}{R\cos\phi}U\frac{\partial U}{\partial \lambda} + \frac{V}{R}\frac{\partial U}{\partial \phi} - \left(\frac{\tan\phi}{R}U + f\right)V = -\frac{1}{R\cos\phi}\frac{\partial}{\partial \lambda}\left[\frac{p_s}{\rho_0} + g(\zeta - \alpha\eta)\right] + \frac{\nu_T}{H}\frac{\partial}{\partial \lambda}\left[\frac{\partial UH}{\partial \lambda} + \frac{\partial UH}{\partial \phi}\right] + \frac{\tau_{s\lambda}}{\rho_0 H} - \tau_* U, \quad \text{and} \tag{2}$$

$$\frac{\partial V}{\partial t} + \frac{1}{R\cos\phi}U\frac{\partial V}{\partial \lambda} + \frac{V}{R}\frac{\partial V}{\partial \phi} + \left(\frac{\tan\phi}{R}U + f\right)U = -\frac{1}{R}\frac{\partial}{\partial \phi}\left[\frac{p_s}{\rho_0} + g(\zeta - \alpha\eta)\right] + \frac{\nu_T}{H}\frac{\partial}{\partial \phi}\left[\frac{\partial VH}{\partial \lambda} + \frac{\partial VH}{\partial \phi}\right] + \frac{\tau_{s\phi}}{\rho_0 H} - \tau_* V, \tag{3}$$

where

t = time,
λ, ϕ = degrees longitude and latitude,
ζ = the free-surface elevation relative to the geoid,
U, V = the depth-averaged horizontal velocities,
$H = \zeta + h$ = the total water column,
h = the bathymetric depth relative to the geoid,
$f = 2\Omega \sin\phi$ = the Coriolis parameter,
Ω = the angular speed of the earth,
p_s = the atmospheric pressure at the free surface,
g = acceleration due to gravity,
η = the Newtonian equilibrium tide potential,
α = the effective earth elasticity factor,
ρ_0 = the reference density of water,
$\tau_{s\lambda}$, $\tau_{s\phi}$ = the applied free-surface stress,
$\tau_* = C_f[(U^2 + V^2)^{1/2}/H]$ = the bottom friction term,
C_f = the nonlinear bottom friction coefficient, and
ν_T = the depth-averaged horizontal eddy viscosity coefficient.

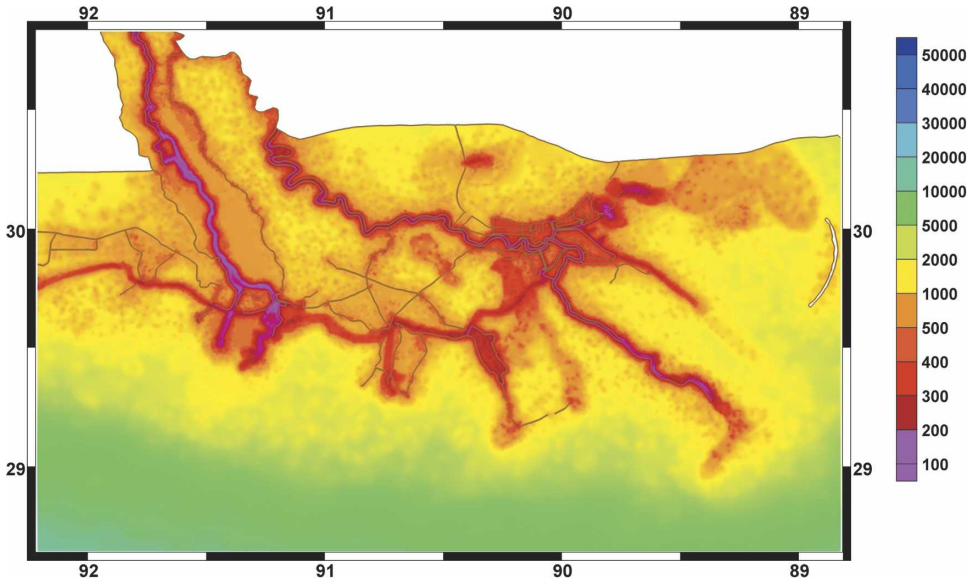

FIG. 8. Finite-element sizes (m) for the S08 grid in southeastern LA.

b. Parameterization of subgrid-scale processes

A hybrid friction relationship is used that varies the bottom-friction coefficient with the water column depth:

$$C_f = C_{f\min}\left[1 + \left(\frac{H_{\text{break}}}{H}\right)^{\theta_f}\right]^{\gamma_f/\theta_f}. \quad (4)$$

This formulation applies a depth-dependent, Manning-type friction law below the break depth (H_{break}), and a standard Chezy friction law when the depth is greater than the break depth (Luettich and Westerink 1999, 2006a). The parameters are set to $C_{f\min} = 0.003$, $H_{\text{break}} = 2.0$ m, $\theta_f = 10$, and $\gamma_f = 1.3333$.

Momentum diffusion and dispersion due to unresolved lateral scales of motion and the effects of depth averaging are accounted for by an eddy viscosity closure model. A horizontal eddy viscosity, $\nu_T = 50\ \text{m}^2\ \text{s}^{-1}$, was found to accurately model flow-stage relationships in the Mississippi and Atchafalaya Rivers as well as the

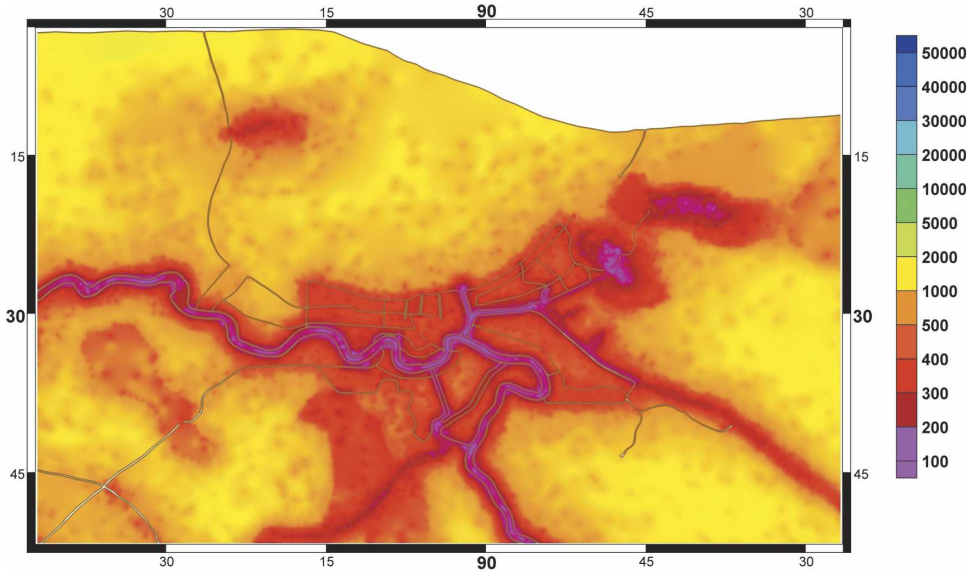

FIG. 9. Finite-element sizes (m) for the S08 grid across metropolitan New Orleans and Lake Pontchartrain.

tidal exchange in the Lake Pontchartrain–Lake Borgne system through the Rigolets and Chef Menteur Pass. Free lateral slip is allowed at all land boundaries and at the wet–dry element interfaces because lateral boundary layers cannot be resolved at the defined grid scales and no-slip conditions unrealistically restrict flows with the defined grids and lateral eddy viscosity values (Feyen et al. 2002).

Levee, road, and railroad systems that act as barriers to flood propagation are features that generally fall below the defined grid scale and often experience strong vertical acceleration and result in a three-dimensional nonhydrostatic flow. ADCIRC defines these weirs as internal barrier boundaries using pairs of computational nodes on opposite sides of the features with a specified crown height (Leendertse 1987; Westerink et al. 2001; Luettich and Westerink 2006a,b). Once the water level reaches an elevation that exceeds the crown height, flow across the structure is computed using basic weir formulas. Weir conditions also are implemented for external barrier boundaries, which permit surge that overtops levee structures at the edge of the domain to transmit flow out of the computational area.

c. Wetting and drying

ADCIRC applies a wet–dry algorithm that is applicable to a continuous Galerkin finite-element discretization that utilizes Lagrange basis functions with nodally defined variables (Luettich and Westerink 1999; Dietrich et al. 2006). The wet–dry algorithm is based on a combination of nodal and elemental criteria. The algorithm requires all nodes within an element to be wet in order for hydrodynamic computations to be calculated at that element. Two parameters are used to define the wetting–drying criteria. First, H_0 defines the nominal water depth for a node to be considered wet. Second, a minimum velocity, $U_{\min}$, is specified that must be exceeded for water to propagate from a wet node to a dry node. Nodes are defined as initially dry if they lie above the defined starting water level or if they are within predefined regions, such as those surrounded by ring levees (e.g., New Orleans).

The algorithm proceeds through the following steps to update the wet and dry elements for the next time level. Wetting is accomplished by examining each dry element with at least two wet nodes with depth greater than 1.2 H_0 (ensuring sufficient water depth to sustain flow to the adjacent node). The velocity of the flow from the wet nodes toward the dry node along each element edge is computed based on a balance between the surface gradient and friction. If this velocity exceeds $U_{\min}$, then the third node and the element are wetted. Finally, a check is made for elements that are bordered by elements with wet nodes but with insufficient water column height (not greater than 1.2 H_0) that they were not toggled wet themselves. If they exist, they are implicitly wet due to the fact that the wet–dry algorithm is nodal. However, an elemental check ensures that elements that do not meet the wetting criteria are forced dry. For hurricane storm surge inundation, wet–dry parameters that are relatively unrestrictive have been found to be most effective: $H_0 = 0.10$ m and $U_{\min} = 0.01$ m s^{-1}. It is critical that all wet–dry checks be done at a small enough time interval so that the wetting–drying algorithm is not Courant surpassing. This latter condition artificially retards the wetting front as the surge progresses inland and the surge height will artificially build up behind the wetting front. Practically, this implies performing wet–dry checks at each model time step and ensuring that the time step taken is not Courant surpassing.

d. Tidal and riverine forcing functions and steric effects

The open-ocean boundary is forced with the K_1, O_1, M_2, S_2, and N_2 tidal constituents; interpolating tidal amplitude; and phase from Le Provost's Finite Element Solutions (FES95.2) global tidal model (Le Provost et al. 1998). Tidal potential forcing incorporating effective earth elasticity factors for each constituent are applied on the interior of the domain for the same constituents (Westerink et al. 1992, 1994a; Mukai et al. 2002). The nodal factor and equilibrium argument for boundary and interior domain forcing tidal constituents are determined based on the starting time of the simulation.

The resonant characteristics of the Gulf of Mexico require a period of model simulation in order for the startup transients to physically dissipate and for the dynamically correct tidal response to be generated. The model is run with tidal forcing for a minimum of 18 days before hurricane forcing so that the tidal signal becomes effectively established; this spinup time was determined through testing of model sensitivity to the generation of resonant modes using separate single semidiurnal and diurnal tidal constituents. A hyperbolic tangent ramp function is applied to the first 12 days of the tidal forcing to minimize the generation of startup transients.

At land boundary nodes outside of southern Louisiana, a no-normal flow condition is applied. At land boundaries in southern Louisiana, external barrier boundaries are specified. At river boundaries, a simple elevation or flux boundary condition would reflect tides and surge waves that are propagating upriver back into the domain. To prevent this nonphysical reflection from occurring, a wave radiation boundary condition

was developed that specifies flux into the domain while allowing surface waves to propagate out (Flather and Hubbert 1990; Luettich and Westerink 2003). This river radiation boundary condition is based on linearly partitioning normal flow on the river boundary into a part due to the river flow, q_{river}, and a part due to waves, q_{wave}, that includes tides and storm surge:

$$q_N = -q_{\text{river}} + q_{\text{wave}}. \tag{5}$$

Using the analytical relationship for the celerity of a linear surface gravity wave,

$$q_{\text{wave}} = c\,\zeta_{\text{wave}}, \tag{6}$$

where the speed of the gravity waves is approximated by

$$c = \sqrt{gH},$$

the normal boundary flux, q_N, becomes

$$q_N = -q_{\text{river}} + c\,\zeta_{\text{wave}}. \tag{7}$$

Noting that the perturbation due to surge and tides is approximated by

$$\zeta_{\text{wave}} = \zeta - \zeta_{\text{river}}, \tag{8}$$

where ζ_{river} equals the surface elevation of the river at the boundary due to the river flow alone, q_{river}. The resulting radiation condition is then based on the relationship between the normal flow and the elevation at the boundary:

$$q_N = -q_{\text{river}} + c(\zeta - \zeta_{\text{river}}). \tag{9}$$

Equation (9) is then used to evaluate the total normal boundary flux due to all flow. Thus, the calculation of the surge elevation requires prior knowledge of the river flow, q_{river}, as well as the elevation associated with the river flow, ζ_{river}, without any tides and/or surge. For a specified river flow, q_{river}, the model is run to obtain the river-flow-only response, ζ_{river}. The fully forced simulation with tides, winds, and waves then proceeds with q_N being computed with the river flow data, q_{river} and ζ_{river}, and an explicit evaluation of the total water elevation, which includes tides, wave, and surge, ζ. The computed normal flow q_N at the radiation boundary is then used in the model. River inflows to the Mississippi River at Tarbert Landing and to the Atchafalaya River at Simmesport are specified as a flux per unit width using gauge data values averaged over the time of the storm. A 2-day spinup period with a 0.5-day hyperbolic ramping function is applied to the river boundary forcing prior to any additional model forcing. This allows for a dynamic steady state in the rivers to be established prior to interaction with any other forcing terms to properly define the pretide and prestorm river stages on the boundaries, ζ_{river}.

Finally, seasonal thermal expansion of the Gulf waters due to baroclinic processes and radiational heating are included implicitly by applying a steric adjustment to the initial and boundary conditions. This expansion is captured in tidal data analyses and appears in the long-term solar annual and semiannual (Sa and Ssa) harmonic constituents. Examination of the harmonic constants computed by NOAA for stations across southern Louisiana shows that the amplitudes of the Sa and Ssa constituents are, on average, just over 18.6 cm. It is assumed that the hurricanes generally take place in the late summer and early fall when the seasonal thermal expansion is at its largest. Therefore, the water levels are adjusted by the addition of the maximum steric level of 18.6 cm.

e. Atmospheric forcing functions

The wind surface stress is computed by a standard quadratic drag law:

$$\frac{\tau_{s\lambda}}{\rho_0} = C_d \frac{\rho_{\text{air}}}{\rho_0} |W_{10}| W_{10-\lambda} \quad \text{and} \tag{10}$$

$$\frac{\tau_{s\phi}}{\rho_0} = C_d \frac{\rho_{air}}{\rho_0} |W_{10}| W_{10-\phi}. \tag{11}$$

Here, W_{10} is the wind speed sampled at a 10-m height over a 10-min time period (Hsu 1988). This wind speed accounts for the adjustment of the wind boundary layer to local roughness directionally, for the level of local inundation, and for forested canopies. The drag coefficient, C_d, is defined by Garratt's drag formula (Garratt 1977):

$$C_d = (0.75 + 0.067W_{10}) \times 10^{-3}. \tag{12}$$

Two methods are used to provide meteorological forcing: a data-assimilative hurricane wind model and a model that solves the governing equations for atmospheric flow within the planetary boundary layer.

The H*WIND model assimilates all available observations of wind speed and direction during the storm, composites these relative to the storm's center, and transforms them to a common reference condition [10-m height, peak (1-min-averaged) wind speed, and marine exposure] (Powell and Houston 1996; Powell et al. 1996, 1998). The hurricane's pressure field is defined by a parametric relationship (Holland 1980). Spatial linear interpolation is used to project wind model output from structured wind grids onto the unstructured ADCIRC grid. The H*WIND model produces snapshots of the storm conditions at hourly or bihourly in-

tervals. Eulerian space–time interpolation between two adjacent snapshots leads to an artificial weakening of the storm (wind stress is reduced by as much as 60%) for times in between the H*WIND defined snaps. This effect is especially pronounced for fast-moving storms due to the wide separation between adjacent snapshots. Therefore, a Lagrangian interpolation scheme has been implemented that tracks the storm's location in time between the defined wind field snapshots. This provides accurate forward motion of the storm along its track, and the 20-min wind fields produced by the scheme do not lead to artificial weakening of the storm. Finally, the 1-min-averaged H*WIND winds are adjusted to a 10-min-averaging period required by the surface drag law by multiplying by a factor of 0.893 (Powell et al. 1996).

We also apply the planetary boundary layer (PBL) model to develop input wind and pressure fields (Cardone et al. 1992; Cardone et al. 1994; Thompson and Cardone 1996). The model is based on the equations of horizontal motion, vertically averaged through the PBL, and is driven by specification of the storm location, minimum central pressure ($p_{\min}$), and maximum wind speed. We apply track data from the National Hurricane Center best track developed from poststorm data analysis for hurricane hindcasts and interpolate these data to 2-hourly values. Model output consists of a wind speed and a pressure field on a regular nested mesh centered at the storm's eye every 20 min. These data are then interpolated onto the ADCIRC unstructured grid. We note that the 20-min PBL output intervals do not necessitate the use of the Lagrangian interpolation scheme. The 30-min-averaged PBL winds are adjusted to the 10-min-averaging period required by the surface drag law by multiplying by a factor of 1.04 (Powell et al. 1996).

We have implemented directional land-masking procedures that reduce the wind speed produced by the hurricane wind field models, which assume open-ocean marine conditions, to account for the higher surface roughness that exists over land, the level of local inundation, and the presence of dense forested canopies. Thus, the H*WIND and PBL wind models result in marine wind speeds, $W_{10\text{-marine}}$, that must be adjusted to account for local roughness conditions, resulting in W_{10}, which is the wind speed used in the wind stress relationships [Eqs. (10) and (11)].

The wind boundary layer depends on roughness conditions upwind of the location since the boundary layer does not adjust to a new roughness instantaneously. This upwind effect is particularly important in the nearshore region where winds are traveling either off- or onshore and transitioning to or from open marine conditions. A land-masking procedure that does not account for wind direction would incorrectly produce full marine winds in the nearshore zone when winds come from land and result in reduced marine winds overland when winds come off the water. Accurate winds are critical in these nearshore and low-lying overland regions that experience either drawdown or flooding because the wind stress term in the shallow-water equations is inversely proportional to the total-water column height, and thus the sensitivity to these winds is the greatest.

Land roughness in overland regions is characterized by land-use conditions such as urban, forested, agricultural, or marsh as described by the USGS National Land Cover Data Classification raster map based upon Landsat imagery (Vogelmann et al. 2001) and USGS Gap Analysis Program (GAP) data (National Wetlands Research Center 2006). This information is then combined with land roughness lengths, $z_{0_{\text{land}}}$, defined by the Federal Emergency Management Agency (FEMA) HAZUS software program (Federal Emergency Management Agency 2006). It is noted that we applied only land-use/cover data that describe present-day land-use/cover and applied this to all modeled storms since historical land-use/cover data were incomplete. Directional roughness values, $z_{0_{\text{land-directional}-k}}$, are computed for each node in the ADCIRC computational grid for 12 upwind directions as a weighted average of the roughness lengths for all pixels in the USGS land classification raster image that are within 30 km upwind of the computational node. The weighted pixel land roughness $z_{0_{\text{land}}}$ values upwind of the computational node are added together to get the weighted upwind land roughness coefficient for the $k = 1, 12$ directions:

$$z_{0_{\text{land-directional}-k}} = \frac{\sum_{i=0}^{n} w(i) z_{0_{\text{land}}}(i)}{\sum_{i=0}^{n} w(i)}, \tag{13}$$

where n equals the number of upwind pixels within 30 km of the point of interest and the weighting parameter is defined by

$$w(i) = \frac{1}{\sqrt{2\pi}\sigma} e^{[-d(i)^2/2\sigma^2]}, \tag{14}$$

where $d(i)$ is the distance from the computational node to the pixel and σ determines the importance of the closest pixels and is set to 6 km. We note that the exponential weighting factor reduces rapidly beyond a distance σ.

The directional changes in surface roughness from open marine conditions do not fully characterize the

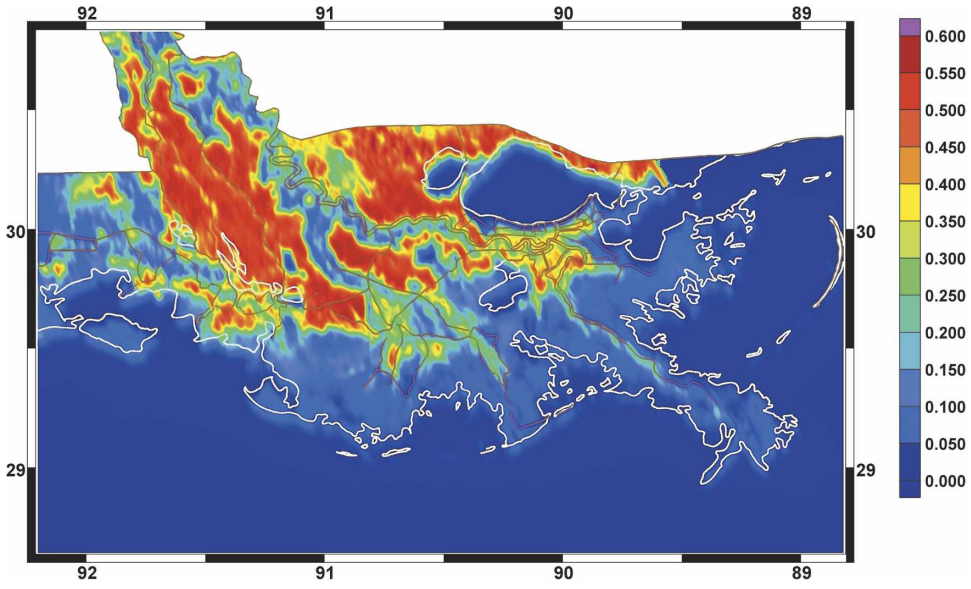

FIG. 10. Directional roughness length $z'_{0_{\text{land-directional}-k}}$ throughout southeastern LA for a northerly wind. Raised features are shown in brown and the position of the normal coastline is outlined in white.

changes in surface stress on the water column during storm surge inundation. As inundation takes place, the land roughness elements (e.g., marsh grass, crops, bushes) are slowly submerged and the drag is reduced. Therefore, the overland roughness length is reduced in the model depending upon the local water column height and assuming that the physical roughness height is 30 $z_{0_{\text{land}}}$ (Simiu and Scanlan 1986). The reduced roughness length $z'_{0_{\text{land-directional}-k}}$ is limited to the marine roughness value, which is reached as the water depth H increases:

$$z'_{0_{\text{land-directional}-k}} = z_{0_{\text{land-directional}-k}} - \frac{H}{30} \quad \text{for}$$

$$z'_{0_{\text{land-directional}-k}} \geq z_{0_{\text{marine}}}, \tag{15}$$

where the open marine roughness, $z_{0_{\text{marine}}}$, can be computed based on the Charnock relationship (Charnock 1955) and the relationship between the friction velocity and the applied drag law (Hsu 1988):

$$z_{0_{\text{marine}}} = \frac{0.018 C_d W^2_{10-\text{marine}}}{g}. \tag{16}$$

The wind reduction factor, $f_{\text{r-directional}}$, is now calculated for each of the 12 directions as a ratio between the surface roughness for open marine conditions $z_{0_{\text{marine}}}$ and the weighted upwind land roughness adjusted for local inundation. The approximation of the wind speed reduction is based on applying a power law approximation to logarithmic boundary layer theory (Powell et al. 1996; Simiu and Scanlan 1986):

$$f_{\text{r-directional}-k} = \left(\frac{z_{0_{\text{marine}}}}{z'_{0_{\text{land-directional}-k}}} \right)^{0.0706}. \tag{17}$$

Actual wind reduction factors used at each node during the simulation are determined from the precomputed directional roughness values closest to the wind direction at that time and place. The adjusted wind speeds used in the wind stress formulas, Eqs. (6) and (7), are then computed from the H*WIND and PBL marine wind speeds as

$$W_{10} = f_{\text{r-directional}-k} W_{10_{\text{marine}}}. \tag{18}$$

Figures 10 and 11 present directional roughness $z_{0_{\text{land-directional}-k}}$ values for southeastern Louisiana. These figures illustrate the differing effects on roughness for winds coming off and onto land in nearshore regions. For the northerly wind in Fig. 10, the directional roughness extends offshore along the northern shore of Lake Pontchartrain as well as along the coast of western Louisiana while marine roughness actually extends to within New Orleans on the south shore of Lake Pontchartrain. For the southerly wind in Fig. 11, marine roughness now extends onshore for the north shore of Lake Pontchartrain and the coast of central Louisiana while a significant shadow zone extends over Lake Pontchartrain from the south shore. There is also a significant difference for these two wind directions along Plaquemines Parish with the roughness being characterized by the open water from which the winds originate.

Finally, the application of the directional wind speed adjustments accounts for how the wind boundary layer is affected but does not characterize how the wind pen-

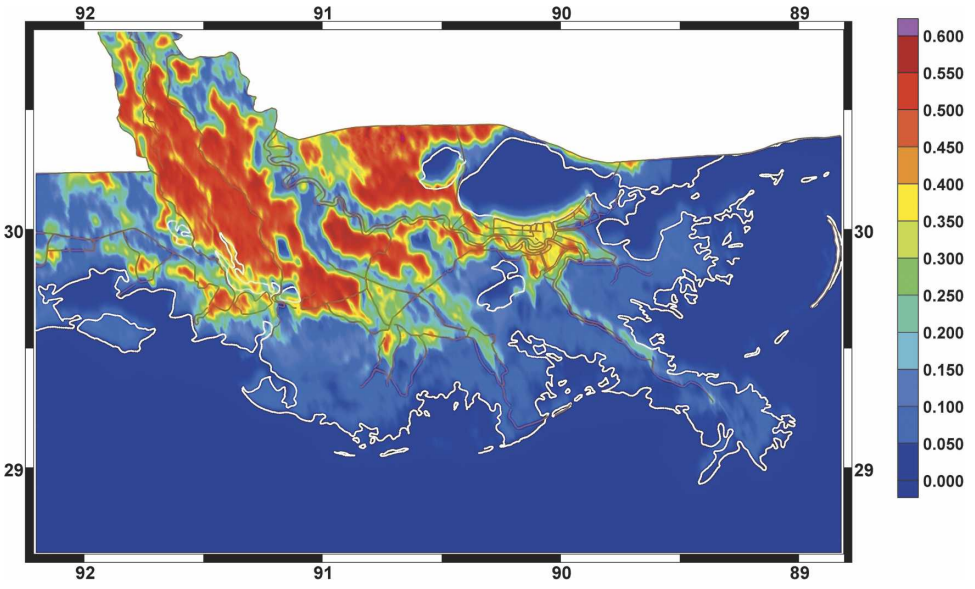

FIG. 11. Directional roughness length $z'_{0_{\text{land-directional}-k}}$ throughout southeastern LA for a southerly wind. Raised features are shown in brown and the position of the normal coastline is outlined in white.

etrates the physical roughness elements. There are large-scale features, such as heavily forested canopies, that shelter the water surface from the wind stress and in effect create two-layered systems. It can be demonstrated that little momentum transfer occurs from the wind field to the water column in heavily canopied areas (Reid and Whitaker 1976). Therefore, in heavily canopied regions where USGS land-use maps define a roughness length greater than 0.39 (except for urban areas), no wind stress is applied at the water surface. The forested canopied areas in southeastern Louisiana are shown in Fig. 12.

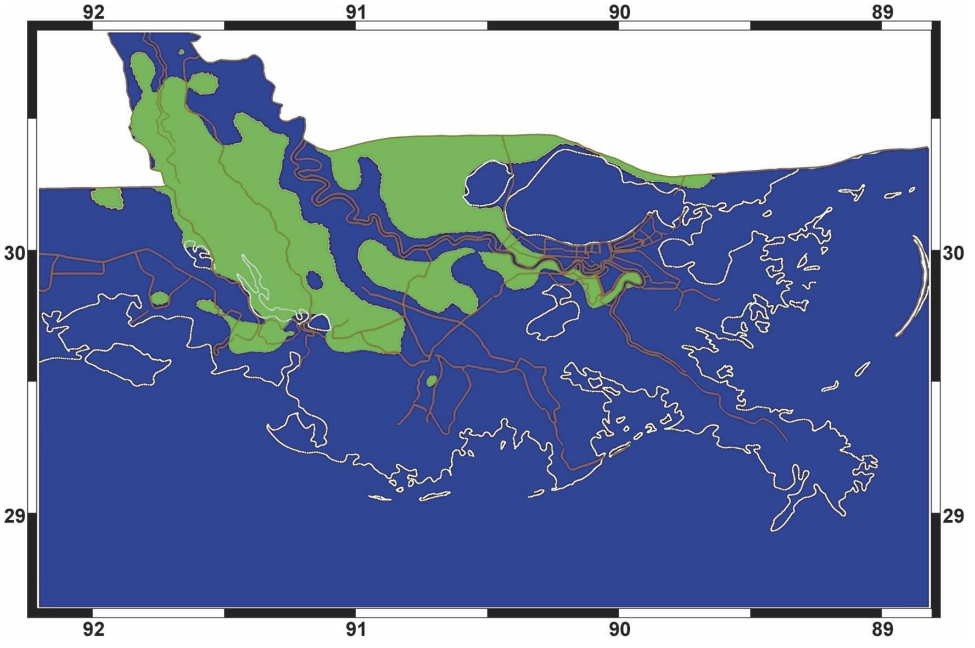

FIG. 12. Forested canopied areas (shown in green) in southeastern LA as determined by USGS land-use data. Raised features are shown in brown and the position of the normal coastline is outlined in white.

TABLE 2. List of hydrograph data locations available from the USACE and USGS for Hurricanes Betsy and Andrew. USACE data for Betsy are from U.S. Army Engineer District, New Orleans (1965), USACE data for Andrew were obtained from the U.S. Army Engineer District, New Orleans (2002, personal communication), and USGS data for Andrew are available from Lovelace (1994).

Description	Longitude (°)	Latitude (°)	Betsy	Andrew	
			USACE	USACE	USGS
East Fork tributary near Cameron	−93.332 778	29.828 333			X
North Calcasieu Lake near Hackberry	−93.299 444	30.031 667			X
Freshwater Bayou Lock South	−92.305 833	29.552 500			X
Freshwater Canal above Beef Ridge	−92.305 278	29.555 000		X	
ICW at Leland Bowman Lock East	−92.194 444	29.783 333		X	
Cypremort Point	−91.881 667	29.713 889			X
Luke's Landing	−91.543 056	29.596 667	X		
Mud Lake	−91.609 400	29.755 800	X		
Wax Lake outlet at Calumet	−91.372 778	29.697 778			X
Wax Lake outlet at Calumet	−91.368 611	29.702 500		X	
Bayou Teche at West Calumet Floodgate	−91.375 278	29.703 611		X	
Six Mile Lake near Verdunville	−91.393 056	29.763 611		X	
Wax Lake East Control Structure South	−91.322 778	29.640 833		X	
Eugene Island	−91.381 667	29.379 167		X	
Round Bayou at Deer Island	−91.262 778	29.474 444		X	
Lower Atchafalaya River below Sweet Bay Lake near Morgan City	−91.244 722	29.551 667			X
Bayou Boeuf Lock East on ICW	−91.173 611	29.683 056		X	
Lower Atchafalaya River at Morgan City	−91.210 833	29.694 444	X	X	
Grand Lake at Charenton	−91.523 889	29.905 556		X	
Chicot Pass at West Fork Chicot Pass	−91.485 556	30.060 833		X	
Bayou La Rompe at Lake Long	−91.588 333	30.224 722		X	
Blind Tesas Cut below Upper Grand River	−91.565 000	30.240 556		X	
Bayou Beouf at Amelia	−91.097 222	29.668 333		X	
Houma Navigation Canal at Dulac	−90.729 722	29.385 000			X
Dulac	−90.715 370	29.389 640			X
Lake tributary to Lake Boudreaux SW of Chauvin	−90.621 667	29.426 944			X
Bayou Lafourche at Leeville	−90.208 889	29.247 778		X	
Bayou Blue near Catfish Lake	−90.346 944	29.391 944		X	
Grand Bayou tributary west of Galliano	−90.422 222	29.455 556			X
Barataria Pass east of Grand Isle	−89.941 667	29.275 278	X	X	
Barataria Bay north of Grand Isle	−89.946 944	29.419 722			X
Tennessee Canal near cutoff	−90.195 833	29.455 556			X
Little Lake near cutoff	−90.184 167	29.515 556			X
Bayou Barataria at Lafitte	−90.110 000	29.668 333	X	X	
Lareussite Canal near Naomi	−90.016 667	29.691 667			X
Bayou Barataria at Barataria	−90.132 222	29.741 389		X	
Algiers Lock	−89.974 444	29.911 944	X		
South Pass	−89.133 300	29.000 000	X		
Mississippi River at Empire	−89.595 833	29.390 278		X	
Mississippi River at Port Sulphur	−89.689 444	29.477 222		X	
Mississippi River at Pointe-a-la-Hache	−89.796 944	29.571 111	X	X	
Mississippi River at Alliance	−89.969 722	29.685 278		X	
Mississippi River at Algiers Lock	−89.968 990	29.920 799	X		
Mississippi River at Chalmette	−90.003 333	29.945 000	X	X	
Mississippi River at New Orleans (Carrollton)	−90.136 111	29.934 722	X		
Mississippi River at Bonnet Carre	−90.443 056	29.998 611		X	
Mississippi River at Baton Rouge	−91.202 778	30.425 000		X	
California Bay near Sunrise Point northeast of Naim	−89.568 056	29.485 556			X
North California Bay near Pointe-a-la-Hache	−89.583 333	29.516 667			X
NE Bay Gardene near Pointe-a-la-Hache	−89.666 667	29.600 000			X
Black Bay near Snake Island near Pointe-al-la-Hache	−89.566 667	29.633 333			X
Lake Pontchartrain at West End	−90.115 556	30.021 667	X		
IHNC near Seabrook Bridge	−90.032 778	30.029 167	X		
MRGO at Paris Rd.	−89.934 722	30.006 667	X	X	
Bayou Bienvenue at floodgate east	−89.915 278	29.997 778		X	
MRGO at Shell Beach	−89.683 333	29.850 000	X		

TABLE 2. (*Continued*)

Description	Longitude (°)	Latitude (°)	Betsy	Andrew	
			USACE	USACE	USGS
Old Shell Beach	−89.650 930	29.864 820	X		
Lake Pontchartrain at Irish Bayou near south shore	−89.869 167	30.146 111		X	
Chef Menteur Pass near Lake Borgne	−89.806 944	30.067 778		X	
Lake Pontchartrain at Midlake	−90.125 833	30.187 778	X		
Lake Pontchartrain at Mandeville	−90.095 833	30.358 611	X		
Rigolets near Lake Pontchartrain	−89.736 944	30.167 222	X	X	
Rigolets near Slidell	−89.722 222	30.169 444		X	
Biloxi	−88.828 700	30.382 000	X		

f. Finite-element solution to the shallow-water equations

The generalized wave continuity equation (GWCE) solution is the current solution algorithm in ADCIRC. The GWCE is generated by combining the spatially differentiated momentum equation in its conservative form with the temporally differentiated continuity equation and adding the continuity equation multiplied by a numerical parameter τ_0 (Lynch and Gray 1979; Kolar et al. 1994b). The solution is consistent and spatially second-order accurate (Luettich et al. 1992; Kolar et al. 1994a; Westerink et al. 1994b; Luettich and Westerink 1995; Dawson et al. 2006) Comparisons to the functionally equivalent Quassi–Bubble SWE solution provide guidance for the selection of the τ_0 parameter resulting in optimal phase propagation properties (Galland et al. 1991; Atkinson et al. 2004). The optimal value of τ_0 is related to the bottom friction parameter τ_*. In the computations, τ_0 is set to 0.03 in the overland portions of southern Louisiana, to 0.02 in waters shallower than 10 m, and to 0.005 elsewhere.

The solution is implemented using Lagrange linear finite elements in space and three- and two-time-level schemes in time for the GWCE and momentum equations, respectively (Luettich and Westerink 2006b). An implicit time discretization is applied for all linear and some nonlinear terms and an explicit discretization is used for most nonlinear terms. This effectively imposes a Courant restriction on the time-stepping solution. However, since GWCE solutions are always more accurate for a Courant number, $C = \sqrt{gh}\Delta t/\Delta x$, below unity and since our wetting–drying procedure is Courant limited as well, this condition is not restrictive.

ADCIRC performs well on parallel platforms due to the application of a conjugate gradients solver and the implementation of domain decomposition to divide the mesh onto individual processors that communicate using a message passing interface (MPI) protocol. For the hurricane storm surge model with the 314 442-node S08 grid and a 2-s time step, a wall-clock time of 6 min day^{-1} of simulation time is required on 256 CRAY XT3 processors.

4. Model validation

Hurricanes Betsy (1965) and Andrew (1992) are hindcast for model validation. We have specifically chosen strong hurricanes because for these events surge reaches its highest levels with significant inland inundation. Furthermore wind-driven surge is the predominant forcing mechanism, as opposed to a short-crested wind-wave setup, in a shallow shelf area such as the northern Gulf of Mexico (Weaver and Slinn 2004, manuscript submitted to *Coastal Eng.*, hereafter WS). We note that the availability of wind data, hydrographs, and system topographic–bathymetric and land-use data is significantly better for more recent storms. Table 2 lists the available hydrograph data stations for these two storms (U.S. Army Engineer District New Orleans 1965; Lovelace 1994; U.S. Army Engineer District New Orleans 2002, unpublished manuscript).

a. Hindcasting Hurricane Betsy

Hurricane Betsy was a borderline category 5 storm that made landfall near Grand Isle, Louisiana, on late 9 September 1965. The hurricane then traveled northwest between the Atchafalaya and Mississippi Rivers, passing less than 75 km southwest of New Orleans before passing Baton Rouge (Fig. 13). Betsy was a fast-moving storm with a forward speed of 10 m s^{-1}. Storm surge was significant, reaching nearly 5 m and inundating 12 500 km^2, including heavily populated areas around the Mississippi River and eastern New Orleans (Fig. 14; U.S. Army Engineer District New Orleans 1965).

ADCIRC driven by H*WIND winds, atmospheric pressure, tides, and riverine forcing simulates storm surge development and propagation. Wind fields for Hurricane Betsy were constructed from historical data records using H*WIND. Figure 15 shows the H*WIND

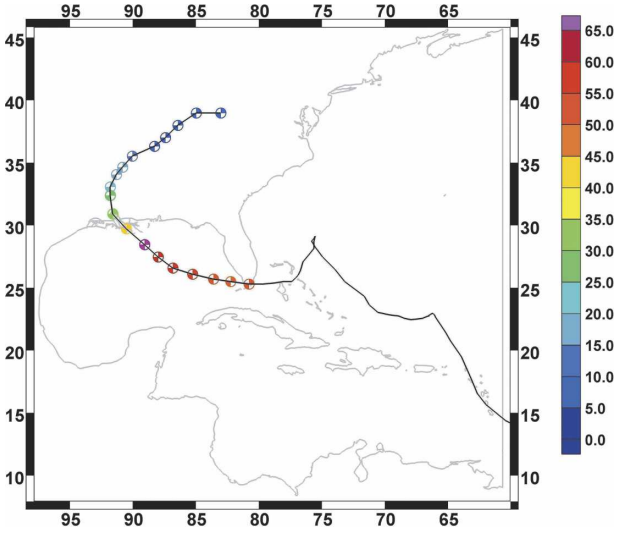

FIG. 13. Hurricane Betsy track data for the time that winds were applied in the ADCIRC simulation between 1200 UTC 8 Sep and 0000 UTC 13 Sep. The position of the eye is given every 6 h. Maximum storm wind speed at each eye position is in m s^{-1} for 10-min-averaged winds.

maximum marine wind velocity adjusted to 10-min-averaged winds. We note some chatter to the west of the track, which is a result of the interpolation interval used to produce the figure. Figure 16 shows the H*WIND maximum applied 10-min-averaged winds adjusted with the directional land-masking algorithm, the inundation algorithm, and the forested canopy factor. We note that to the east of the Mississippi River, the differences between the marine and adjusted winds are due to directional roughness effects along the north shore of Lake Pontchartrain, due to forested canopies around Lake Maurepas and due to roughness effects in the vicinity of English Turn. Due to the wind coming off of open water and the extensive inundation in the region, the overall adjustment of the marine winds was not dramatic in this region. A purely local wind boundary layer adjustment that does not account for flooding would in fact lead to winds in this area that are reduced much more than with our adjustments. To the west of the Mississippi River, surface roughness and canopies substantially alter the marine winds. The adjusted winds are interpolated onto the ADCIRC grid. Nodal factors and equilibrium arguments for the five astronomical forcing tides were computed for the starting time of the simulation: 0000 UTC 18 August 1965. The Mississippi River was forced with a specified flow of 5520 $m^3 s^{-1}$ and the Atchafalaya River was forced with a specified flow of 2200 $m^3 s^{-1}$.

Betsy winds drive Gulf waters across Breton Sound toward the Mississippi River. There is a levee only on the western bank of the Mississippi River for nearly the second half of the river below New Orleans in Plaquemines Parish. This allows surge driven in from Breton Sound to build up in the river and east of the river to more than 4 m. The surge in the river then propagates upstream and passes New Orleans and Baton Rouge at approximately 3.5 m. The same regional surge east of the river also propagates north through Breton Sound and the marshes west of Breton Sound, and is stopped by the Mississippi River levees at English Turn. Water is also blown across from the Gulf into Chandeleur Sound and Lake Borgne, and builds up in the funnel between St. Bernard Parish and New Orleans East, resulting in extensive inundation due to the low levee heights in the area in 1965. Similarly, water levels exceed 4 m in the southwest corner of Lake Pontchartrain, which is in line with the high storm winds coming across the shallow lake. In addition, the high waters on the west side of Lake Borgne coupled with the lowered water levels in eastern Lake Pontchartrain drive flow through Chef Menteur Pass and the Rigolets into Lake Pontchartrain and raise the overall level of the lake. Finally, flooding over Grand Isle into Barataria Bay and the surrounding areas penetrates farthest inland (more than 100 km) to Lac Des Allemands and the surrounding areas, which is just to the southwest of the New Orleans levee system.

The modeled distribution of peak storm surge heights throughout the event is shown for southeastern Louisiana in Fig. 17. Surge typically reaches its greatest heights against the levee structures. The Mississippi River levees in Plaquemines Parish prevent water from propagating from Breton Sound across into Barataria Bay and cause water levels to build up in a large area to the southeast of New Orleans. The levee configuration also contributes to storm surge amplification through a focusing process in this area. The river and levees make a sharp turn at the southeastern edge of New Orleans at English Turn, creating a concave area that amplifies storm surge. The funnel-shaped region between St. Bernard Parish and New Orleans East also effectively amplifies surge. In the western end of Lake Pontchartrain, flow is stopped by a raised railroad and surge exceeds 4 m. The Bonne Carre spillway region is impacted with some of the highest water levels. The extent of modeled flooding in Fig. 17 can be compared to that recorded from Hurricane Betsy by the U.S. Army Corps of Engineers (Fig. 14). The flooded areas compare well: both have widespread flooding around Lake Pontchartrain and Lake Maurepas, in eastern New Orleans and areas east of the Mississippi River, and southwest of New Orleans down to the Gulf of Mexico.

Figure 18 shows the significant effect of the direc-

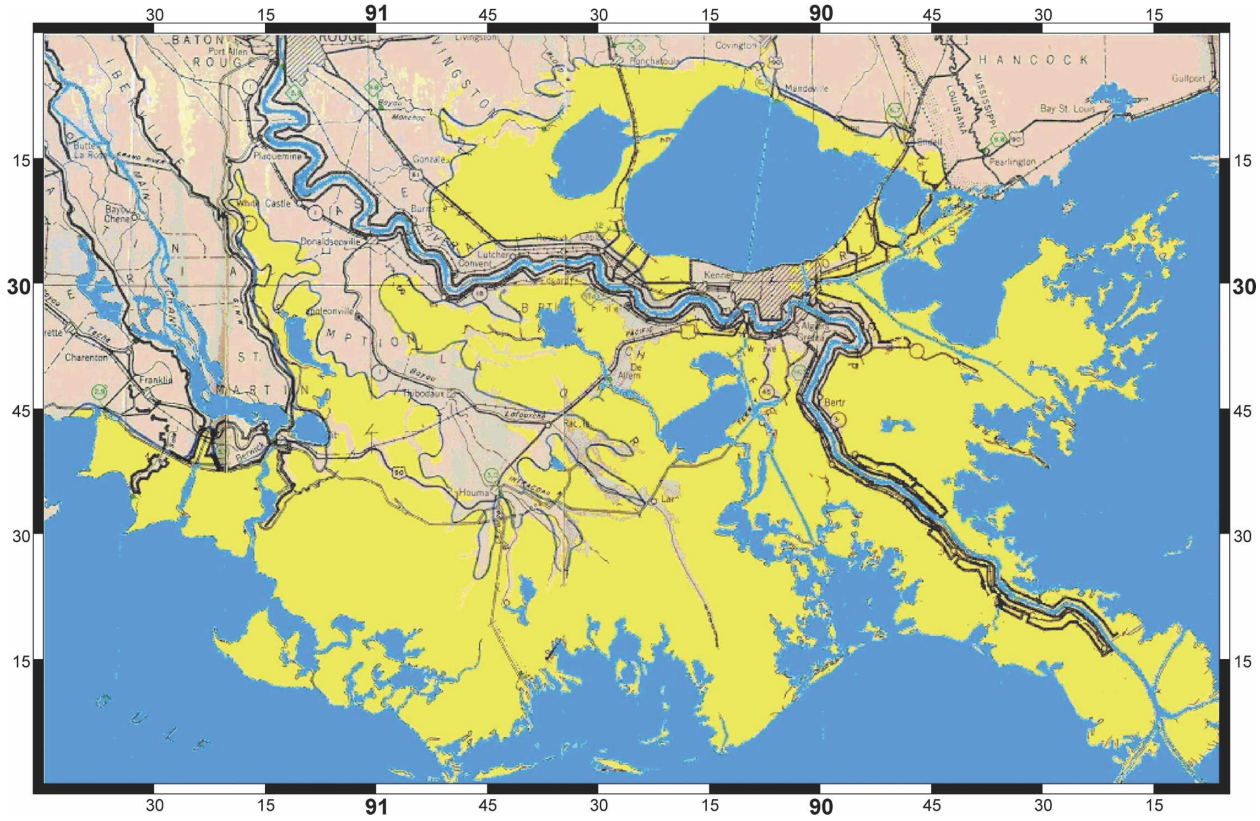

FIG. 14. Recorded inundation from Hurricane Betsy (from U.S. Army Engineer District, New Orleans 1965). Blue indicates water bodies, beige indicates dry land, and yellow indicates normally dry land inundated during Hurricane Betsy.

tional wind reduction algorithm, inundation related wind increases, and canopy reductions on the maximum water levels during the storm. In general, the full marine winds lead to a small reduction of the maximum surge on the order of 5 cm as the winds come across open water; they then build to an increase of 30 cm to more than 1 m as water is pushed up against structures and higher land. The effect of the canopies in the vicinity of Lake Maurepas is particularly strong with the full marine wind leading to more significant nearshore reductions and downwind increases. We note that our combined wind modification algorithm can actually lead to winds that are closer to marine winds in cases such as the wind coming off of open water and when overland inundation occurs, which covers the physical roughness elements. Since Fig. 18 only shows the maximum water levels during the storm, the reduction in low water levels that the algorithm produces is not illustrated.

Differences between the modeled and recorded peak storm surges are calculated in meters at 20 stations where gauges recorded water levels during Betsy (Table 2). These errors are shown on the map of peak modeled errors (Fig. 19). The data record is matched to the modeled water level by examining 0.75 days of record prior to the storm surge signal arriving to account for local data differences in the source data as well as the locally variable subsidence rates. However, this is not possible at all locations due to incomplete data records. The mean error is 0.58 m and the standard deviation is 0.53 m. There are two obvious outliers that are related to missing subgrid-scale features (gates or other controls) and/or vertical datum problems. With these two outliers removed, the mean peak surge error for the remaining 18 data points is reduced to 0.43 m and the standard deviation to 0.31 m.

Time series of the model response during Hurricane Betsy are compared to water-level data at the tidal and river gauges. Hydrographs at 12 stations are plotted with the data records and model output in Fig. 20. The model shows a good match to both the tidal signal and the surge although the surge buildup prior to the peak and dieoff following the peak occur more quickly in the model than in the observations.

b. Hindcasting Hurricane Andrew

Hurricane Andrew struck southern Louisiana near the mouth of the Atchafalaya River at Point Chevreuil

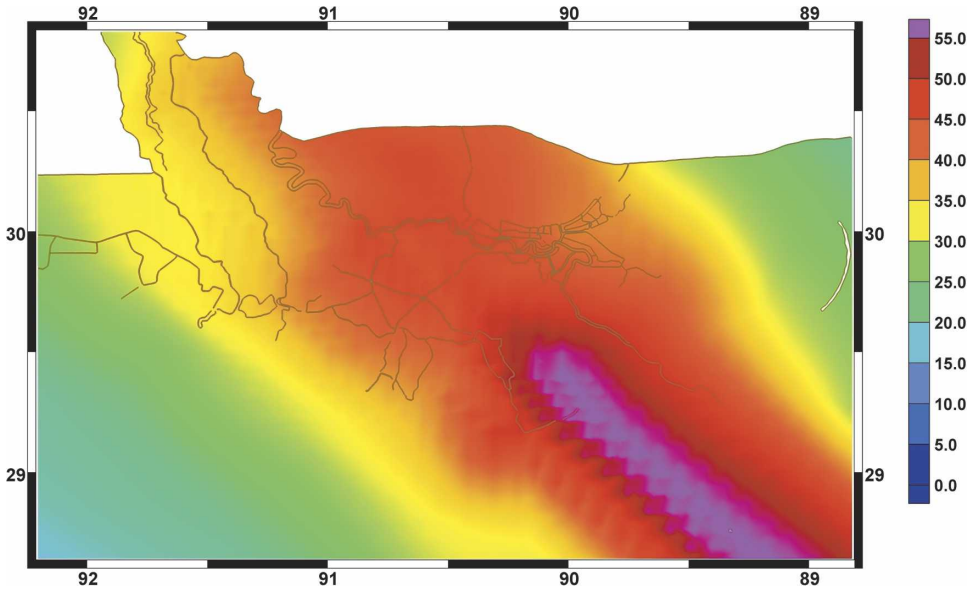

FIG. 15. Hurricane Betsy 10-min-averaged maximum marine wind speed contours from H*WIND ($m\ s^{-1}$) across southeastern LA.

at approximately 0730 UTC on 26 August 1992 as a category 4 storm. The storm made landfall farther west than Betsy but took a more northerly track, passing just to the west of Baton Rouge (Figs. 21 and 22). With a forward speed of approximately 4 $m\ s^{-1}$, Andrew moved slower than Betsy at landfall. The hurricane flooded many unprotected areas around the Mississippi River, Lake Pontchartrain, and within the Atchafalaya River flood basin with its peak surge approaching 2.5 m just east of the eye and 3 m in areas close to New Orleans (Rappaport 2006).

The Hurricane Andrew wind field was reconstructed using the PBL model, based on the storm's track, maximum wind speed, and minimum pressure. Figure 23 shows the maximum 10-min-averaged marine wind speed contours from the PBL model output. Figure 24

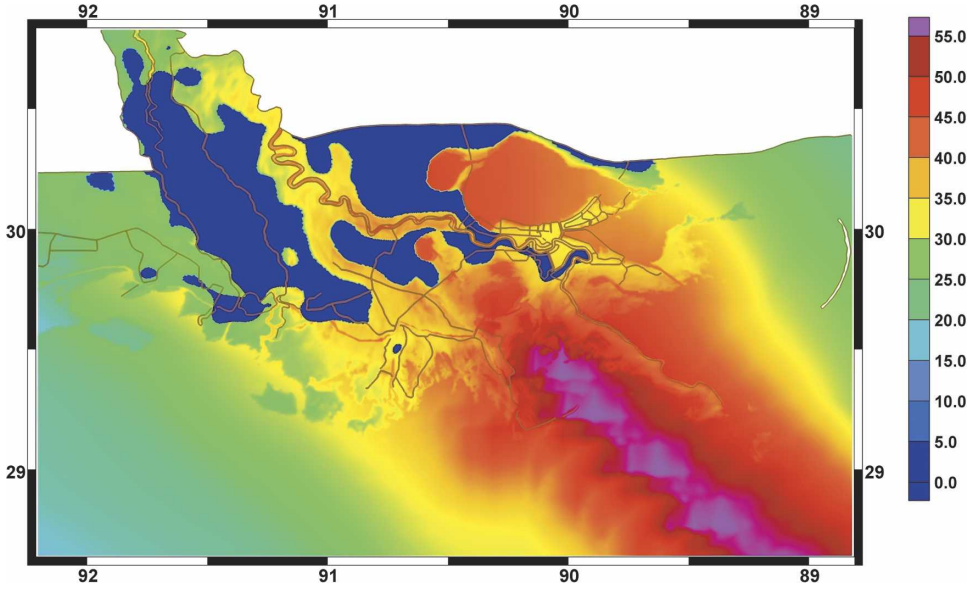

FIG. 16. Hurricane Betsy 10-min-averaged maximum directionally reduced wind speed contours from H*WIND ($m\ s^{-1}$) across southeastern LA.

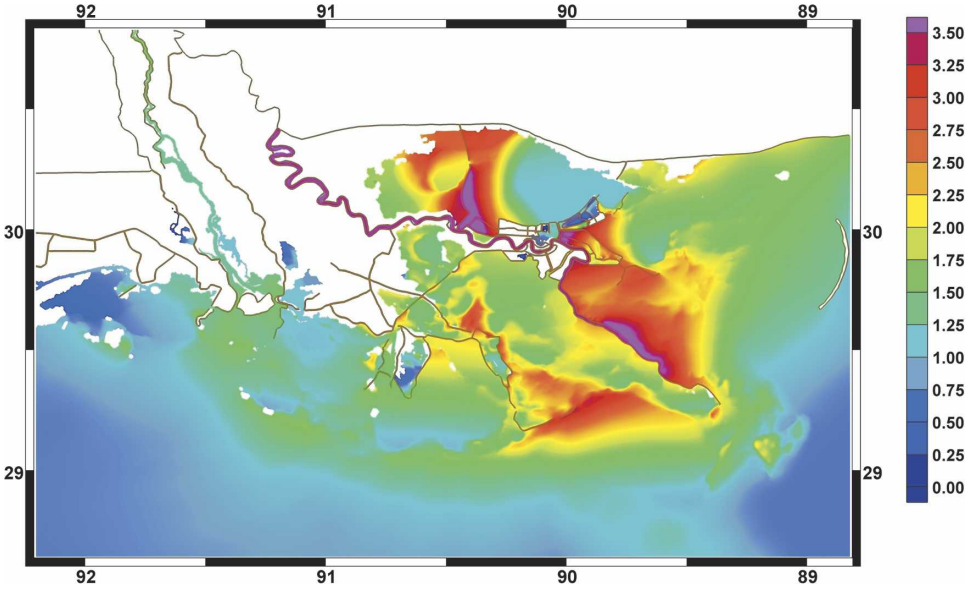

FIG. 17. Hurricane Betsy modeled peak storm surge elevation (m) relative to NGVD29 in southeastern LA computed with directionally reduced winds. Levee structures are shown as brown lines.

shows the PBL maximum applied 10-min-averaged winds adjusted with the directional land-masking algorithm, the inundation algorithm, and the canopy factor. The adjusted PBL model winds are compared to data recorded during Hurricane Andrew to validate the wind model. The recorded data are taken at 12 meteorological stations located at airfields, along the coast, and at offshore buoys (Fig. 22, Table 3). Comparisons between the modeled and recorded wind data are made for wind speed and direction from 25 through 28 August in Figs. 25 and 26. Modeled and measured winds show very good agreement, although small-scale local fluctuations seen in the data record are not reproduced in the modeled winds. We note in Fig. 22 that the comparison anemometers are distributed along the storm track as well as away from the most intense portion of

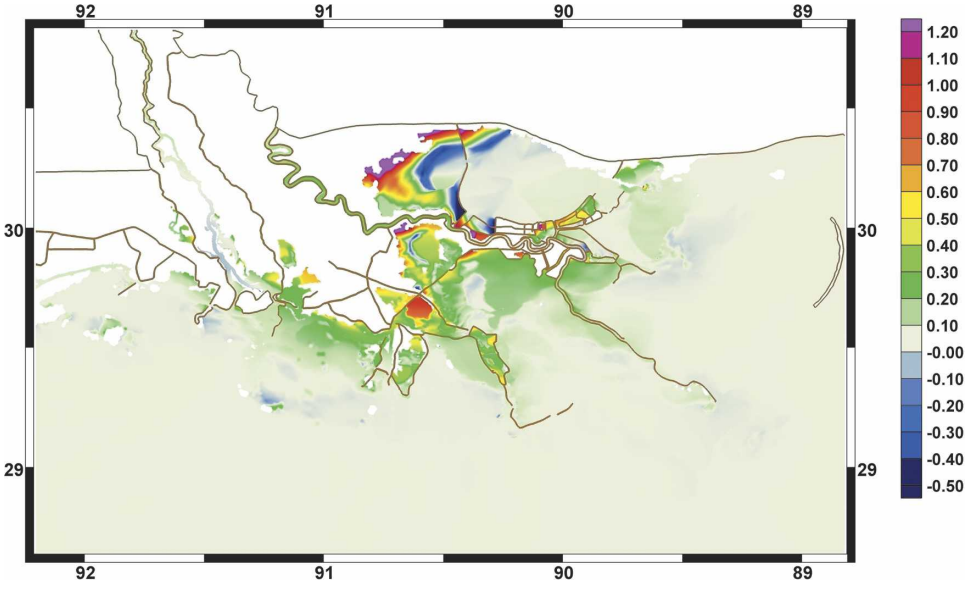

FIG. 18. Difference in Hurricane Betsy modeled peak storm surge elevation (m) in southeastern LA when modeled with marine winds and with directionally reduced winds. Levee structures are shown as brown lines.

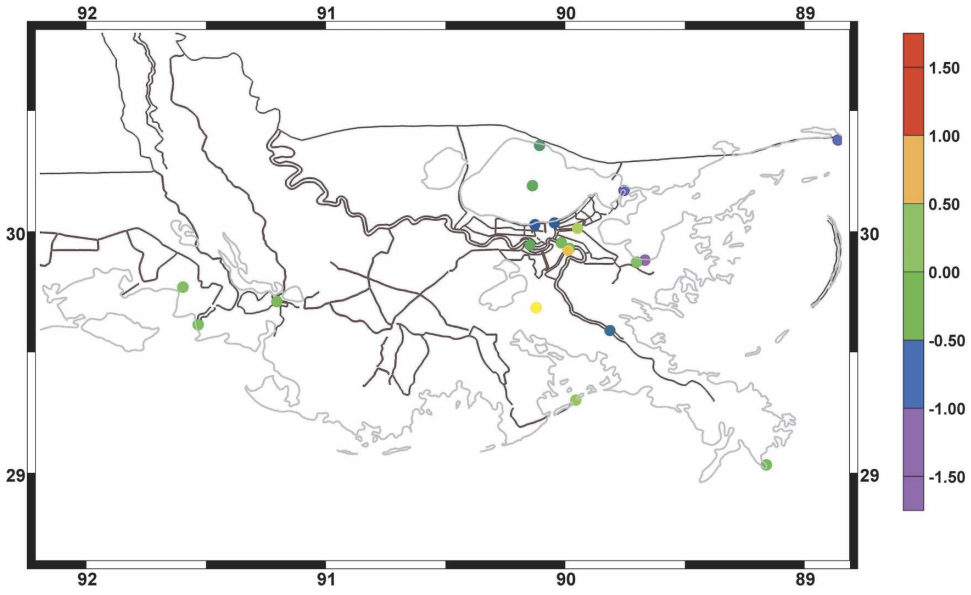

FIG. 19. Hurricane Betsy modeled peak storm surge elevation errors (m) in southeastern LA compared with measured data at 20 stations listed in Table 2. Positive error values indicate model overprediction and negative values indicate underprediction. Levee structures are shown as brown lines.

the storm and are located in open water, inland, and near shore. As such, they indicate that the storm is regionally well captured and that the wind reduction algorithms work well. Nodal factors and equilibrium arguments for the five astronomical forcing tides were computed for the starting time of the simulation: 0000 UTC 4 August 1992. The Mississippi River was forced with a specified flow of 11200 $m^3 s^{-1}$ and the Atchafalaya River was forced with a specified flow of 4850 $m^3 s^{-1}$.

As Andrew first approaches Louisiana, early high surge levels are observed on the eastern side of the Mississippi River levees and Breton Sound, and water is driven into Lake Borgne and Lake Pontchartrain. As the eye makes landfall, it drives surge well above 2 m on its right side while dropping water levels on its left side. The Mississippi River east bank levee system focuses the surge to a peak approaching 3 m at English Turn, as with Betsy. Flooding from Barataria Bay inundates most of the area south of New Orleans and high water is driven into Timbalier and Terrebonne Bays. The main volume of surge inundates most areas south of the GIWW across southern Louisiana. Depths range from 2.5 m near Larose to approximately 1.75 m of surge up the Atchafalaya River. High water levels in Lake Pontchartrain are driven by Andrew's winds to flood much of the northwestern shore. Maximum storm surge contours across southeastern Louisiana are shown in Fig. 27. The surge is highest in areas where the surge builds up against the topographic contours or levee systems. Figure 28 shows the effects of the directional wind reduction algorithm, wind increases with inundation, and wind reductions due to canopies on the maximum water levels during the storm. Again, the full marine winds result in a small reduction of the maximum surge on the order of 5 cm as the winds come across open water, and stage level increases of approximately 30 cm to 1 m are seen as water is pushed up against structures and higher land.

The error in the modeled peak storm surge height is calculated by determining its difference from the recorded maximum surge at 51 gauge stations throughout southern Louisiana (listed in Table 2). These errors are shown with the peak modeled surge in Fig. 29. Prestorm water-level differences between the model and the data record are used to adjust peak surge differences in order to account for vertical datum shifts and local subsidence at individual stations. The mean error in the peak storm surge height is 0.29 m and the standard deviation is 0.28 m. There were two clear outliers due to the errors in the data sources as determined by a comparison to the model output. With these two outliers removed, the mean peak surge error for the remaining 49 stations is 0.27 m and the standard deviation 0.23 m.

Time series of water-level heights from the model during Hurricane Andrew are compared to water-level data from tidal and river gauges. These hydrographs show the progression of the tidal and surge response as the storm evolves. Twelve stations were chosen from the data available during Andrew, and the hydrographs

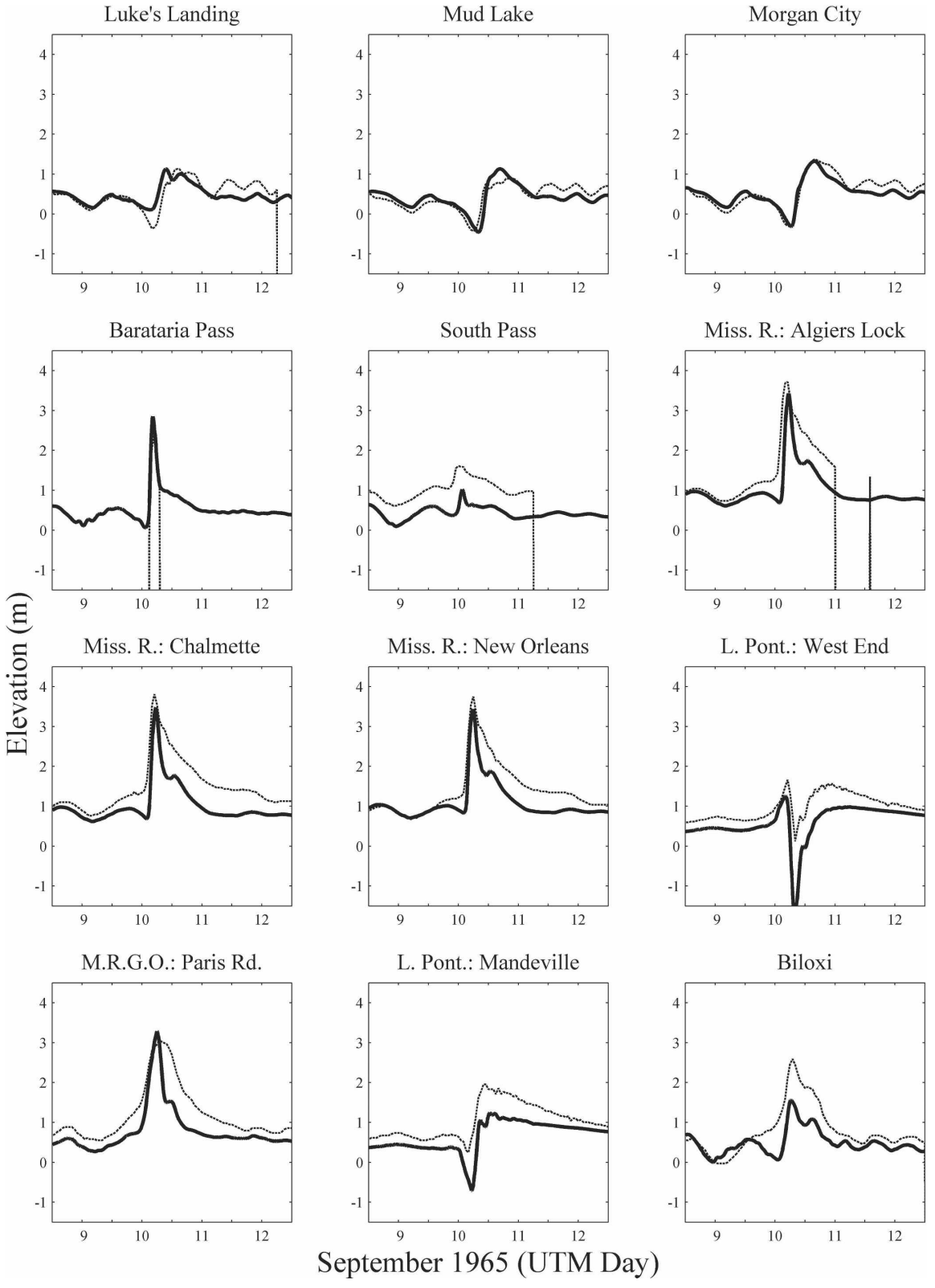

FIG. 20. Hydrographs of modeled (solid line) and recorded (dashed line) water surface elevation (m) relative to NGVD29 during Hurricane Betsy. Dry model response and unavailable data are assigned a value of −99 999.

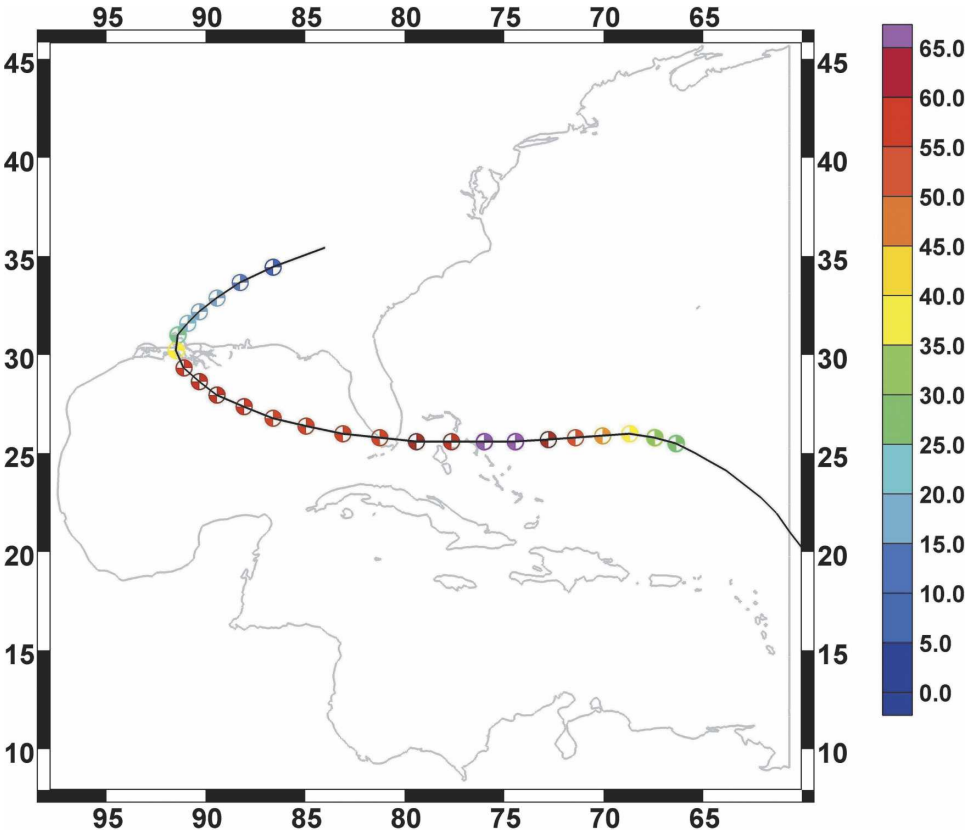

FIG. 21. Hurricane Andrew track data for the time that winds were applied in the ADCIRC simulation between 0000 UTC 22 Aug and 0000 UTC 28 Aug. The position of the eye is given every 6 h. Maximum storm wind speed at each eye position is in m s^{-1} for 10-min-averaged winds.

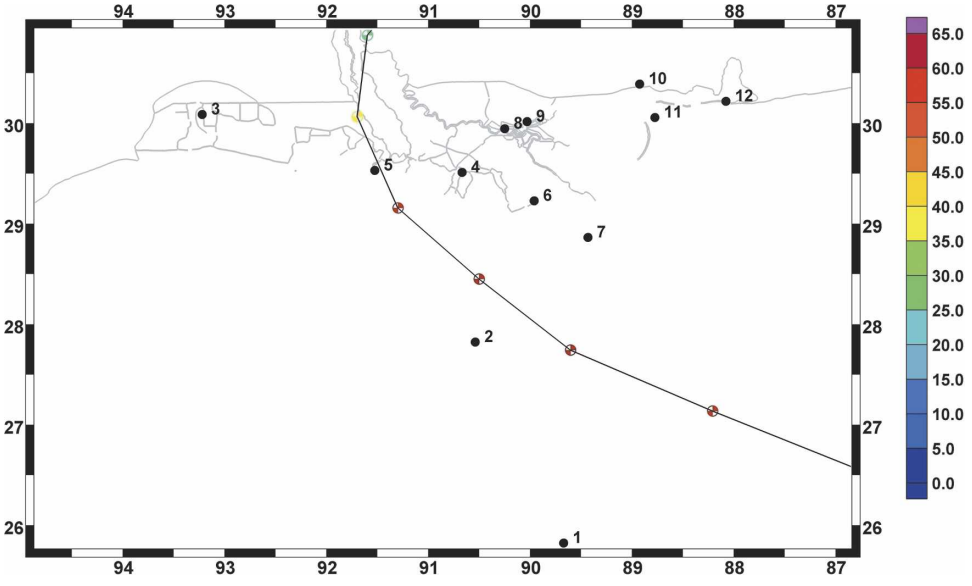

FIG. 22. Detail for Hurricane Andrew track data across the northern Gulf of Mexico. The position of the eye is given every 6 h. Maximum storm wind speed at each eye position is in m s^{-1} for 10-min-averaged winds. Anemometer station numbers listed in Table 3 are indicated.

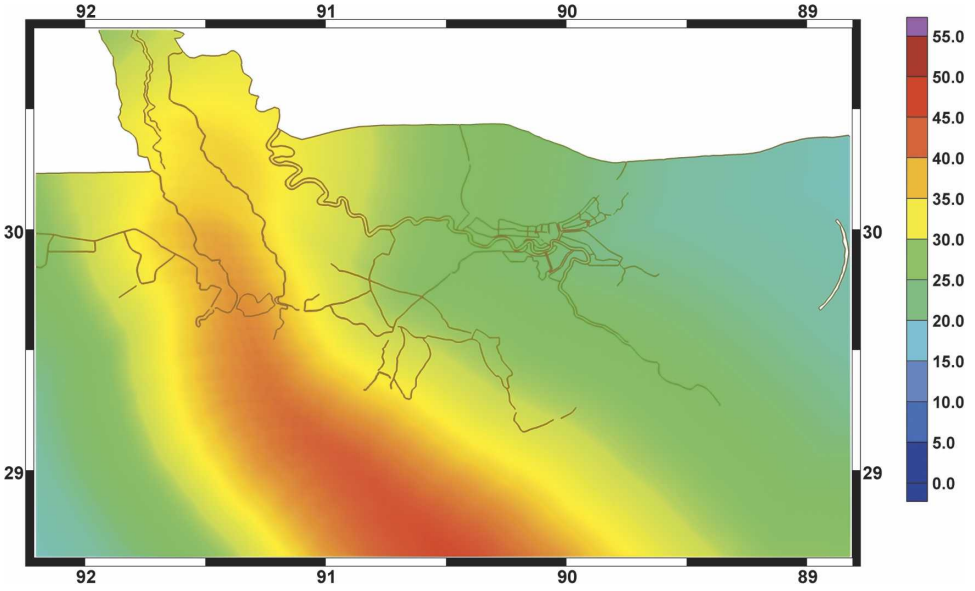

FIG. 23. Hurricane Andrew 10-min-averaged maximum marine wind speed contours from PBL ($m\ s^{-1}$) across southeastern LA.

from the data records and model output are shown in Fig. 30. With the exception of prestorm differences in water levels due to vertical datum errors, the model closely matches the tidal signal and storm surge response.

c. *Assessment of model skill*

Peak modeled storm surge height is compared against the peak recorded storm surge height for Betsy and Andrew in Fig. 31 after adjusting for vertical datum and local subsidence based on prestorm water levels and excluding the four outliers. The slope of the regression line is 0.91, indicating that the model is underpredicting surge by approximately 9%. The correlation coefficient, R^2, is 0.804. Examining Betsy and Andrew individually shows that Andrew's surge more closely matches the recorded surge (slope equals 0.924 versus 0.899).

In Fig. 31, the station data points are divided into five

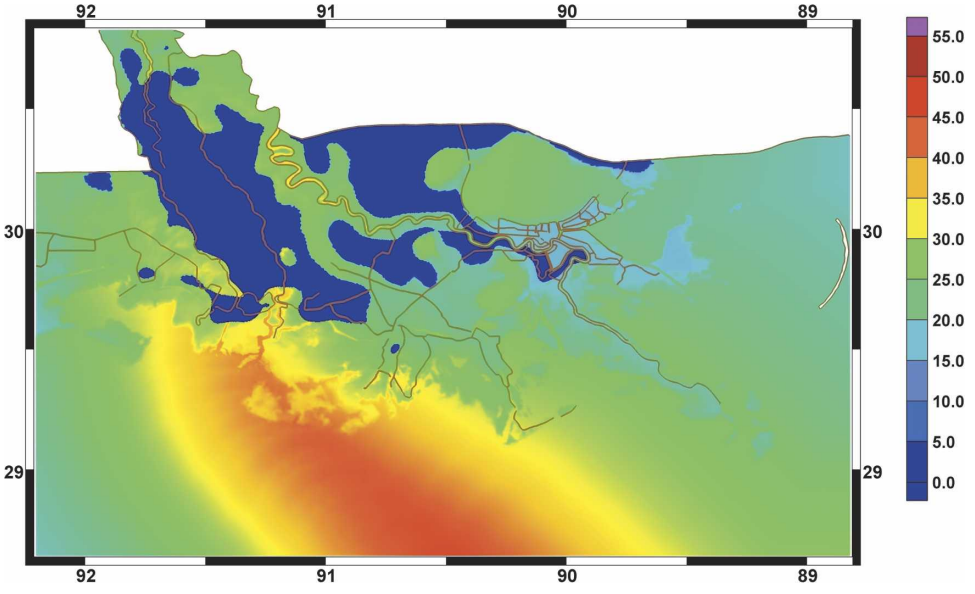

FIG. 24. Hurricane Andrew 10-min-averaged maximum directionally reduced wind speed contours from PBL ($m\ s^{-1}$) across southeastern LA.

TABLE 3. Wind data records during Hurricane Andrew from NOAA Coastal-Marine Automated Network (C-MAN) stations, NOAA National Data Buoy Center (NDBC) buoys (information online at http://www.ndbc.noaa.gov), and NOAA National Climatic Data Center (NCDC) stations (information online at http://www.ncdc.noaa.gov/oa/climate/stationlocator.html).

Name	Source description	Lat	Lon
333 km south of Southwest Pass, LA	NDBC Buoy 42001	25°54′00″N	89°40′00″W
27.88°N, 90.90°W	C-MAN Bullwinkle Block (industry platform)	27°52′48″N	90°54′00″W
Lake Charles	NCDC Lake Charles Regional Airport	30°07′N	93°14′W
Houma	NCDC Houma Terrebonne Airport	29°33′N	90°40′W
Salt Point	NCDC Salt Point, LA	29°34′N	91°32′W
Grand Isle	C-MAN GDIL1	29°16′00″N	89°57′24″W
Southwest Pass	C-MAN BURL1	28°54′18″N	89°25′42″W
New Orleans International Airport	NCDC New Orleans International Airport	29°59′N	90°15′W
New Orleans Lakefront	NCDC New Orleans Lakefront Airport	30°03′N	90°02′W
Keesler AFB	NCDC Biloxi Keesler Air Force Base	30°25′N	88°55′W
40 km SSE of Biloxi	NDBC Buoy 42007	30°05′25″N	88°46′07″W
Dauphin Island	C-MAN DPIA1	30°14′54″N	88°04′24″W

regions that are demarcated by the two main rivers in Louisiana, as river levee systems generally keep the surge from propagating between these regions. Grid resolution is typically poorest in the west, and is best in the New Orleans region and around the Mississippi and Atchafalaya Rivers. Results within the Atchafalaya and, especially, Mississippi Rivers have less variance and tend to be more accurate than in other areas. This indicates that the model is correctly simulating both the surge entering the rivers and surge–tide–current interaction. The model appears to be generally less accurate in the region between the Atchafalaya River basin and the Mississippi River. This area has a significant storm surge response but is not as highly resolved by the model grid nor are the bathymetric and topographic data as complete or reliable in these areas. In addition, there are local features such as levee systems and raised roads that are not represented in the model grid. Examination of the model response east of the Mississippi River, where mesh resolution is highest and most accurate, shows that the model tends to underpredict storm surge, suggesting the model is not incorporating all of the processes contributing to storm surge generation.

To examine the overall characteristics of the model, the differences between the peak and modeled storm surges for Betsy and Andrew at all stations (with the exception of the outliers) are sorted into 0.10-m increments and plotted in a histogram in Fig. 32. While the most frequently occurring errors are between −0.1 and 0.1 m, it is clear that the model tends to generally underpredict the storm surge. Analysis of the differences between the modeled and recorded surge height shows a mean error of −0.15 m, an absolute mean error of 0.30 m, and a standard deviation of 0.37 m.

The most significant factor influencing local model skill is adequate resolution of the hydrodynamic and geographic features. It is likely that the stations with a poor match between the model and observations have surge controlled by features such as local channels, levees, or floodgates that have not been resolved in the model grid. We believe that this is particularly true for the region between the Atchafalaya River basin and the Mississippi River, where we know that the model grid is missing many such small-scale features. In the northern portion of this region, the model surge is too high because there is too much conveyance of water through the areas closer to the open ocean. In the southern portion of this region, there is a systematic underrepresentation of storm surge elevation that may be partly due to the lack of levees and raised roads that cause the surge to pile up in these areas.

Wind waves influence surge height with wind-wave radiation stress, modifying bottom friction, and changing sea surface roughness. Modeling studies have shown that the surge increase due to the wind-wave setup can be proportionally more significant for weaker winds and steep bathymetric profiles (WS). Although wind waves tend to be proportionately less important for strong storms on wide shallow shelves, they do influence the total surge away from the center of the storm, affect the time of arrival of the peak surge, and tend to reduce drawdown. Wind waves reach shore prior to the peak surge driven by the strongest hurricane winds, so the combined wind and wind-wave surge builds up earlier than does the solely wind-driven surge. Furthermore, drawdown caused by winds coming from shore tends to be reduced by waves that are still coming into shore. These factors are consistent with the comparisons of model and observed hydrographs and peak surge that show that the model produces shorter-duration surges and that the percentage of peak surge underprediction is greater for modest levels of storm

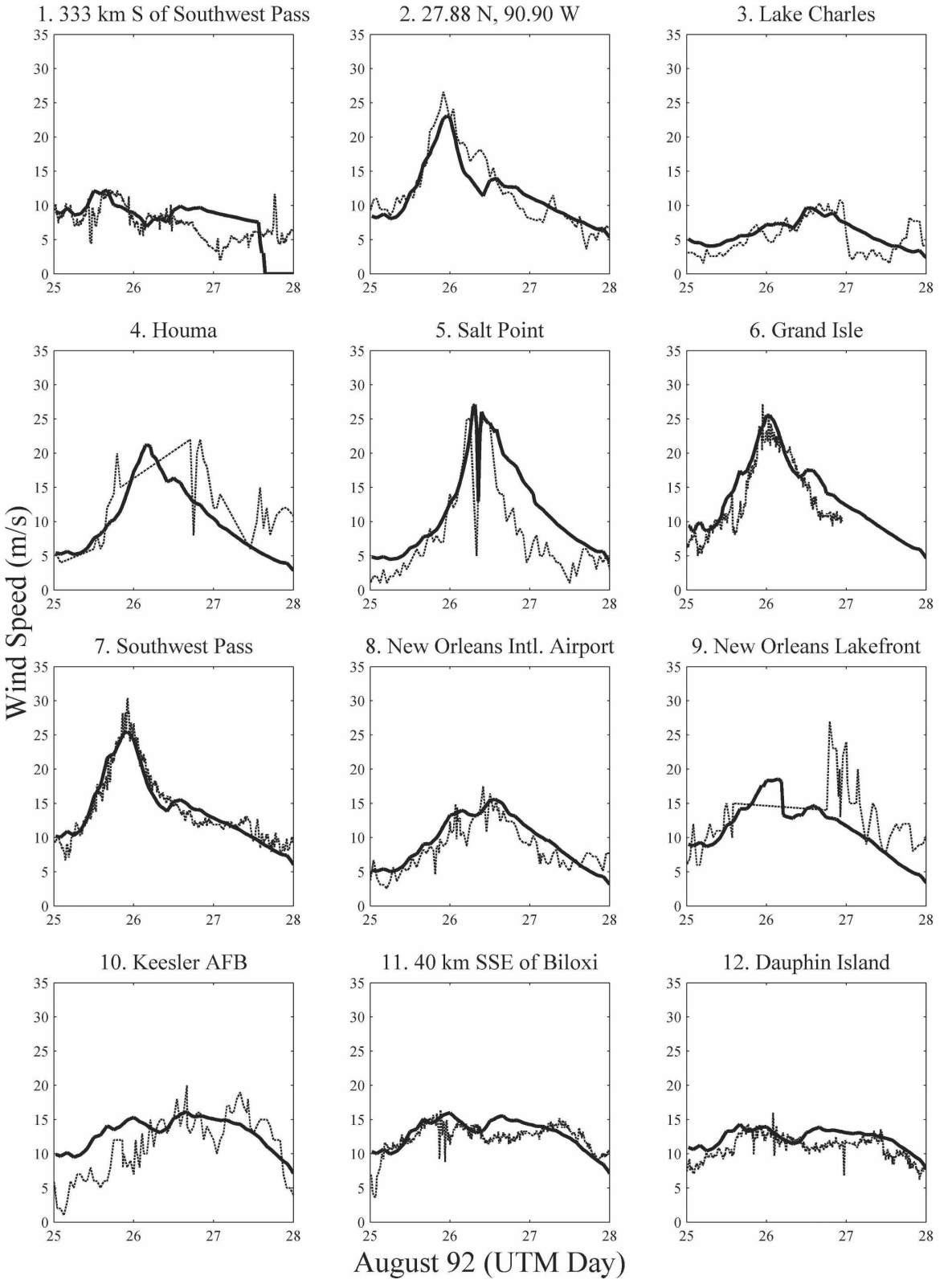

FIG. 25. Modeled (solid line) and recorded (dashed line) wind speed during Hurricane Andrew at the anemometer stations listed in Table 3.

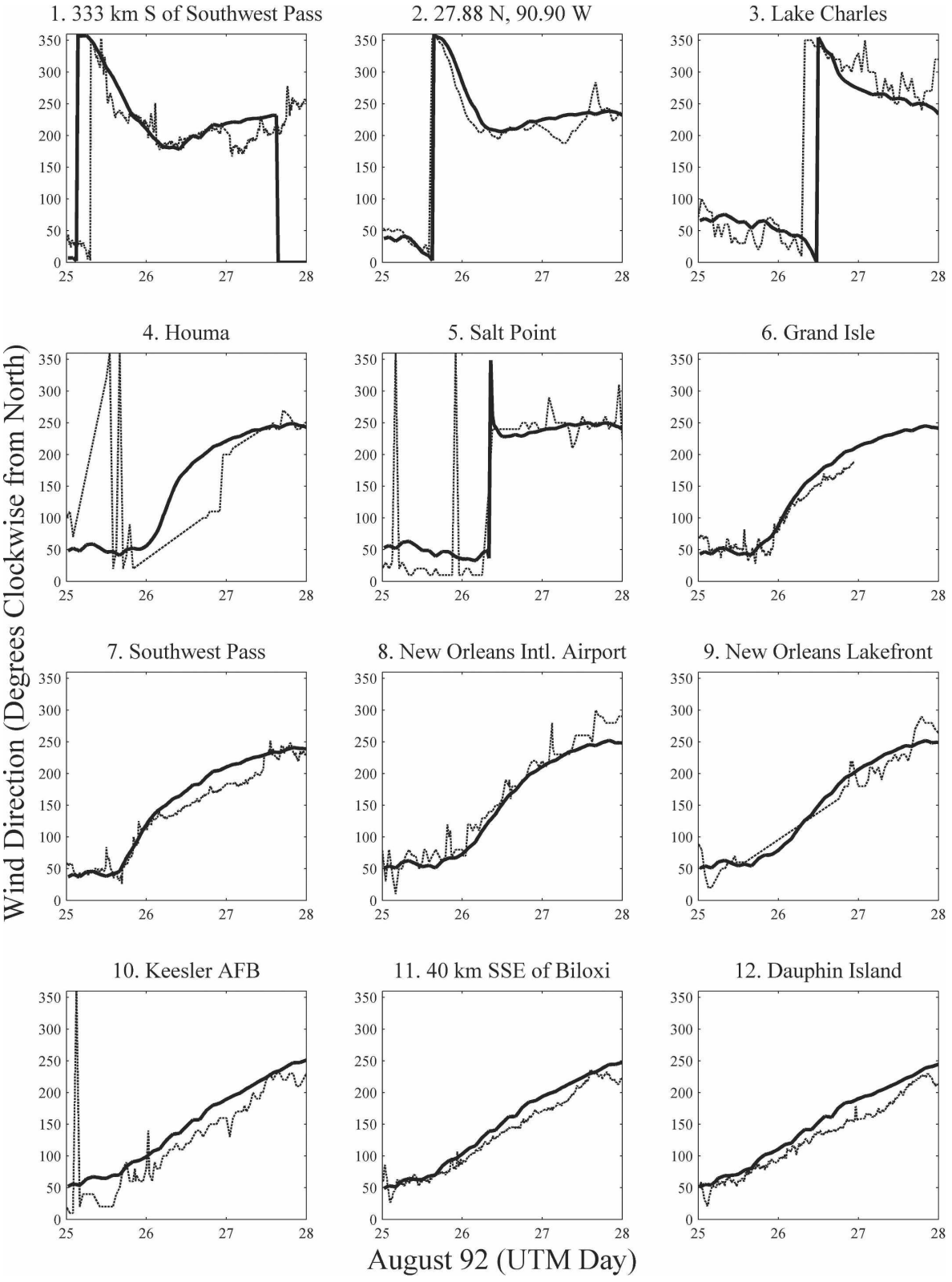

FIG. 26. Modeled (solid line) and recorded (dashed line) wind direction (° clockwise from north) during Hurricane Andrew at anemometer stations listed in Table 3.

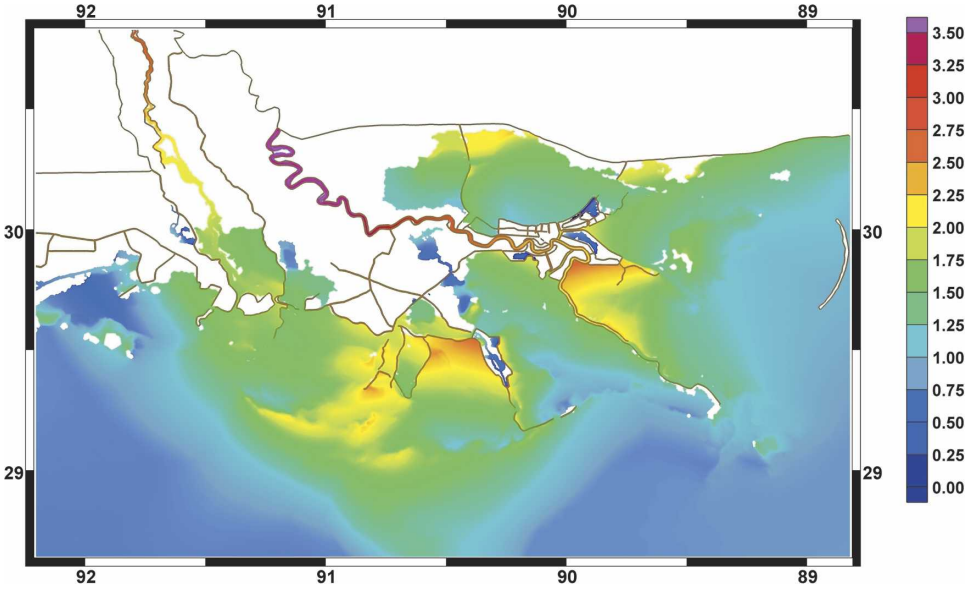

FIG. 27. Hurricane Andrew modeled peak storm surge elevation (m) relative to NGVD29 in southeastern LA computed with directionally reduced winds. Levee structures are shown as brown lines.

surge. In particular, we would expect intensive wave focusing at the foot of the Mississippi River and in the vicinity of the MRGO.

5. Conclusions

In southern Louisiana, storm surge is enhanced by the low-lying delta that protrudes onto the broad and shallow Mississippi–Alabama shelf region. Surge can penetrate far inland through high conveyance waterways and over a low-lying floodplain. A widespread system of levees and raised roadways impedes flow and results in the localized accumulation of high water. This is particularly true for the southern Mississippi River levees that stop flow from moving from east to west across the Mississippi Delta. Surge also tends to be fo-

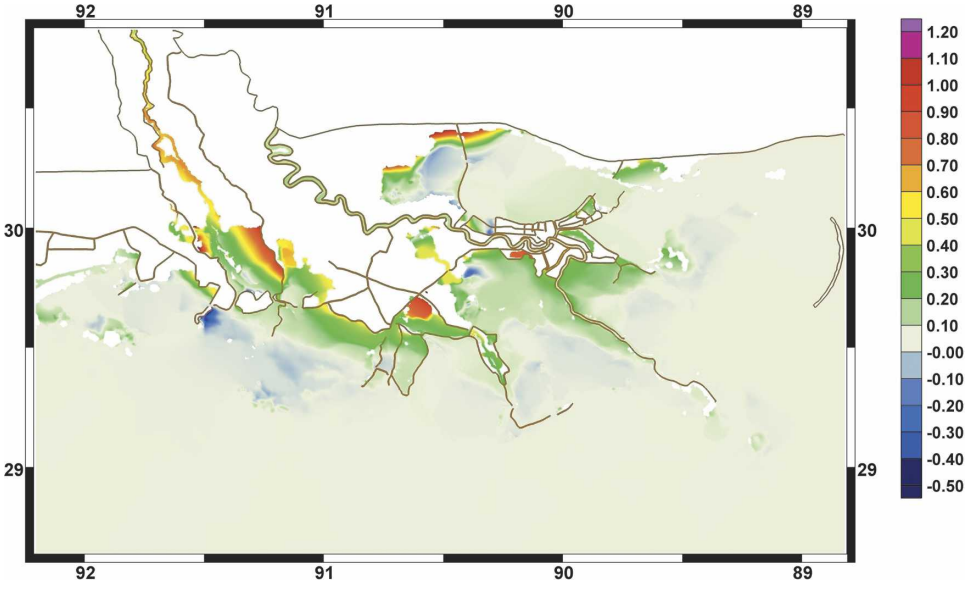

FIG. 28. Difference in Hurricane Andrew modeled peak storm surge elevation (m) in southeastern LA when modeled with marine winds and with directionally reduced winds. Levee structures are shown as brown lines.

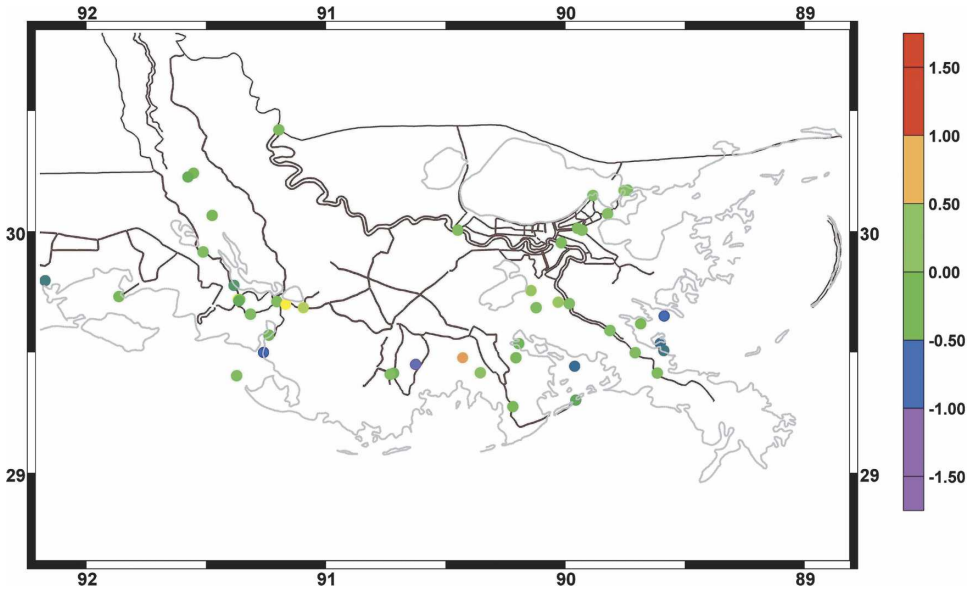

FIG. 29. Hurricane Andrew modeled peak storm surge elevation errors (m) in southeastern LA compared to measured data at 51 stations listed in Table 2. Positive error values indicate model overprediction and negative values indicate underprediction. Levee structures are shown as brown lines.

cused in lateral convergences defined by raised features, such as at English Turn and the funnel between St. Bernard Parish and New Orleans East.

A hydrodynamic model has been developed that resolves the features important to storm surge propagation on a local scale while providing accurate model forcing and parameterization of physical processes. The ADCIRC model uses unstructured grids that provide the resolution of the hydrodynamic and geographic features governing storm surge propagation on a local basis. The domain incorporates the western North Atlantic Ocean, the Gulf of Mexico, and the Caribbean Sea, in order to provide accurate forcing for tides and hurricanes at the open-ocean boundary and inherently captures all significant processes as the storm tracks from the ocean through the resonant Gulf and Caribbean basins and onto the shelf. Within the overland regions, extensive levee systems and raised roadways are incorporated and all significant channels and waterways are represented.

ADCIRC is validated by hindcasting Hurricanes Betsy and Andrew. Modeled water surface elevation was recorded at gauge station locations throughout southern Louisiana for comparison to hydrographic data. These comparisons show the ability of the model to accurately simulate storm surge across Louisiana; the mean peak surge error for Betsy is 0.43 m and for Andrew it is 0.27 m. Comparisons of the modeled to observed peak storm surges show that the model on average lies approximately 10% below the observations.

Despite the well-resolved computational mesh, accurate boundary condition specification and meteorological forcing, and physically realistic parameterizations of surface and subgrid-scale effects, there are areas where the model over- or underpredicts the observed storm surge. We believe there are three areas where it would be helpful to include additional processes contributing to storm surge generation into the model.

First, model errors appear to be associated with regions (e.g., between the Atchafalaya and Mississippi Rivers) where bathymetric and topographic data are sparse and where raised features have not been included in the model grid. Recent lidar-based topographic surveys can be used to better define the topography and the raised features that tend to be impediments to storm surge propagation. In addition, vertical datum definitions should be improved in both the system definition as well as in the observational data allowing for a better representation of the system while also permitting direct comparisons to high water mark data.

Second, the hydrodynamic model is lacking the additional momentum transfer and setup to the storm surge due to short-crested wind waves. This effect becomes relatively more important away from the center of the storm and may contribute a significant portion of the surge height at lower wind conditions. These wind-wave effects are also likely to contribute to water-level setup prior to and following the arrival of peak winds, which are times when our model tends to underpredict water levels. We are in the process of coupling ADCIRC

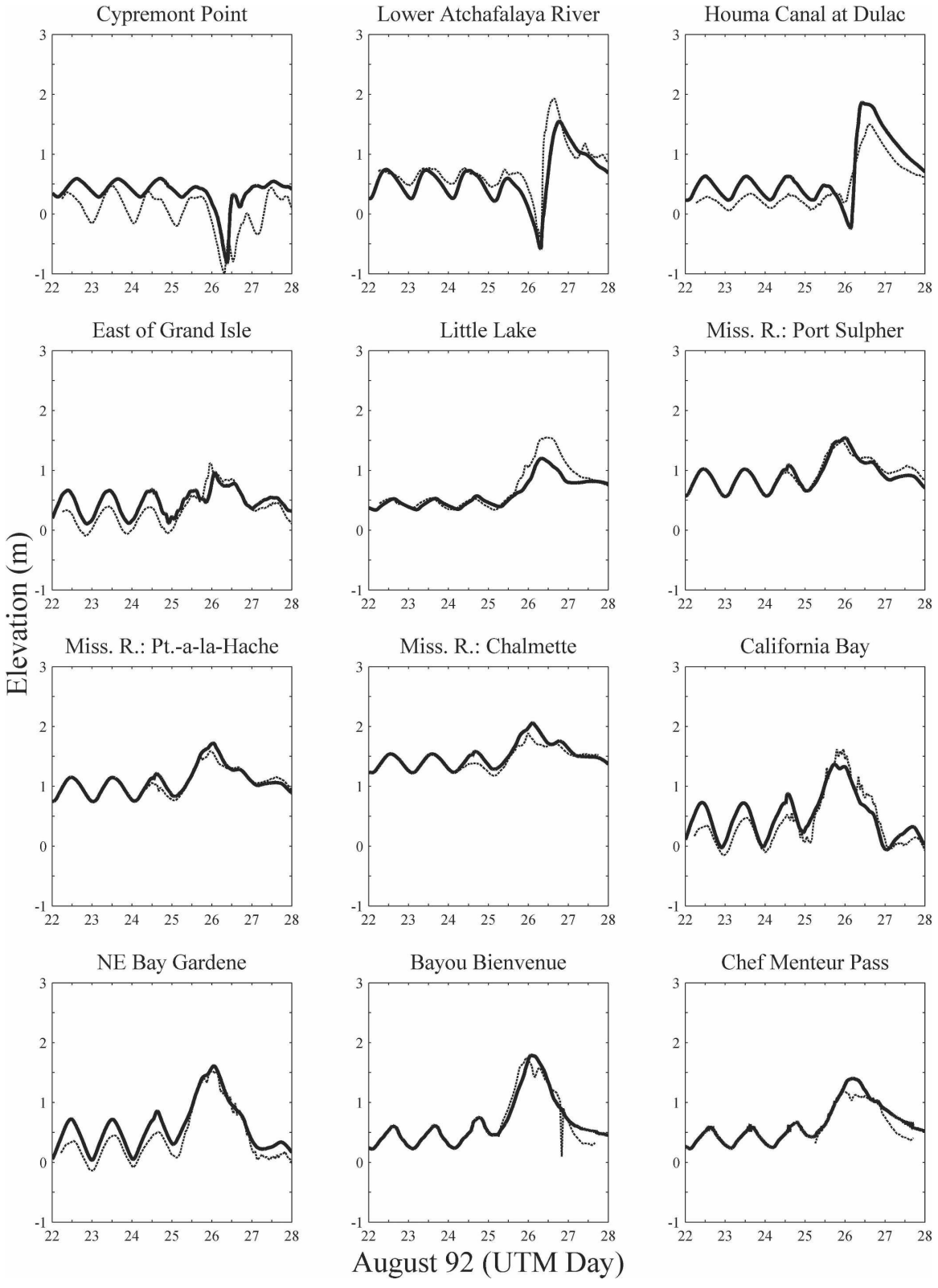

FIG. 30. Hydrographs of modeled (solid line) and recorded (dashed line) water surface elevation (m) relative to NGVD29 during Hurricane Andrew.

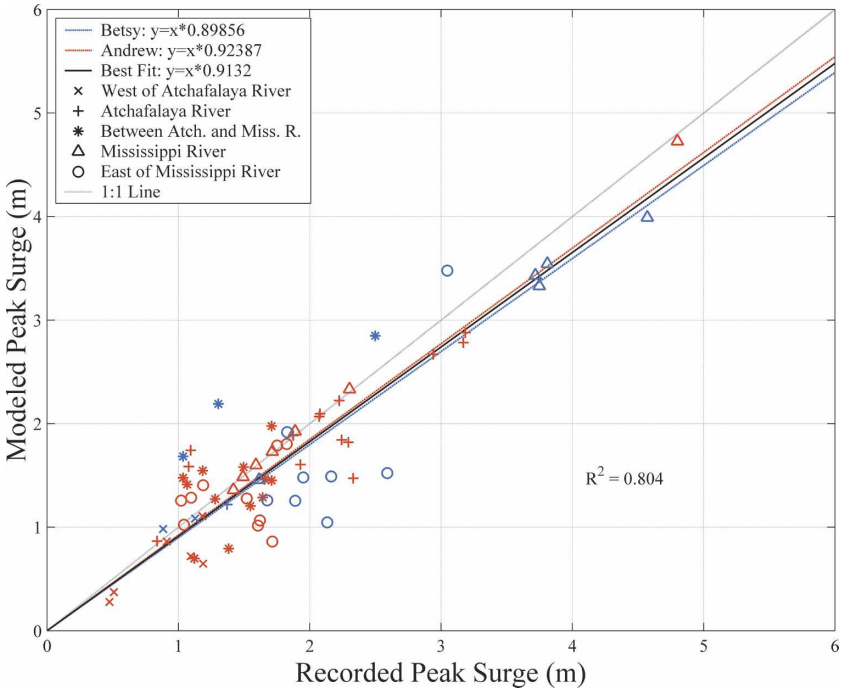

FIG. 31. Comparison of recorded vs modeled peak storm surge elevation (m) from station data listed in Table 2. Betsy results appear in blue and Andrew results in red.

to several wind-wave models to further assess the significance of this forcing.

Third, the application of standard wind drag coefficient relationships may not fully characterize the sea surface roughness and resulting shear stress in a hurricane. There is evidence that a drag coefficient that is solely dependent upon wind speed does not fully describe the actual sea state conditions. The inclusion of a

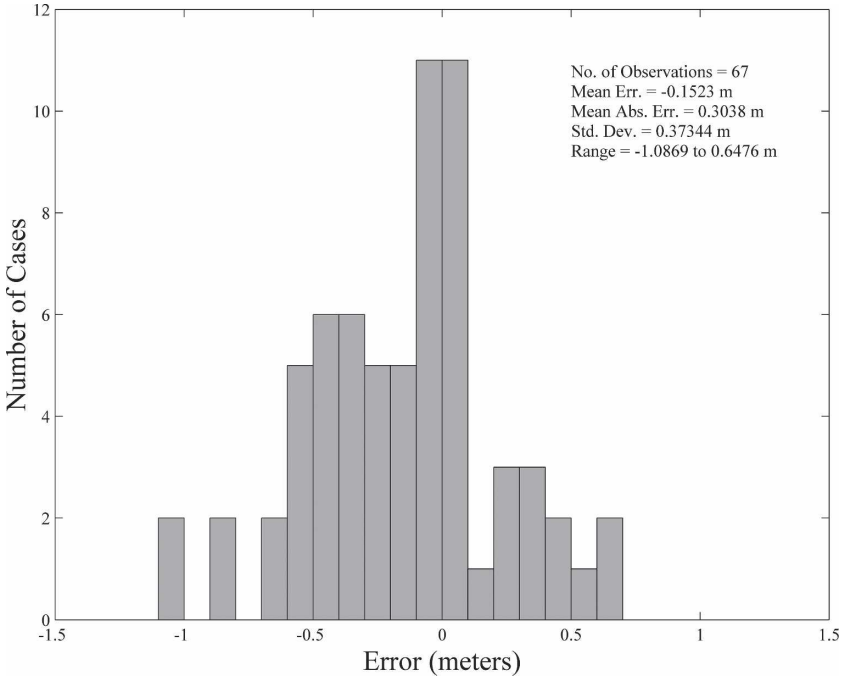

FIG. 32. Histogram of recorded minus modeled peak surge (m) using 67 observations of peak water levels during Hurricanes Betsy and Andrew.

wind-wave model will better define the sea surface roughness and will allow for incorporation of drag coefficient relationships that are dependent upon the wind-wave conditions.

Acknowledgments. We thank Robert G. Dean of the University of Florida at Gainesville and Robert O. Reid of Texas A&M University for their insight and diligent review of our work as part of an external review board for the USACE-MVN. In addition, we thank Harley Winer, Jay Combe, Jay Ratcliff, and Maik Flanagin of the USACE-MVN for significant input.

Funding for the S08 model was provided by the USACE-MVN. In particular, we thank Al Naomi for his strong support of this effort. Funding for ADCIRC code development has been provided by the U.S. Army Engineer Research and Development Center, the National Science Foundation, the Office of Naval Research, the U.S. Naval Research Laboratory, the U.S. Army Research Office, and the Texas Water Development Board.

REFERENCES

Atkinson, J. H., J. J. Westerink, and J. M. Hervouet, 2004: Similarities between the wave equation and the quasi-bubble solutions to the shallow water equations. *Int. J. Numer. Methods Fluids,* **45,** 689–714.

Blain, C. A., J. J. Westerink, and R. A. Luettich, 1994: The influence of domain size on the response characteristics of a hurricane storm surge model. *J. Geophys. Res.,* **99** (C9), 18 467–18 479.

——, ——, and ——, 1998: Grid convergence studies for the prediction of hurricane storm surge. *Int. J. Numer. Methods Fluids,* **26,** 369–401.

Cardone, V. J., C. V. Greenwood, and J. A. Greenwood, 1992: Unified program for the specification of hurricane boundary layer winds over surfaces of specified roughness. Contract Rep. CERC-92-1, U.S. Army Corps of Engineers, 85 pp. + 3 appendixes. [Available from ERDC Vicksburg (WES), U.S. Army Engineer Waterways Experiment Station (WES), ATTN: ERDC-ITL-K, 3909 Halls Ferry Rd., Vicksburg, MS 39180-6199.]

——, A. T. Cox, J. A. Greenwood, and E. F. Thompson, 1994: Upgrade of the tropical cyclone surface wind field model. Miscellaneous Paper CERC-94-14, U.S. Army Corps of Engineers, 27 pp + 4 appendixes. [Available from ERDC Vicksburg (WES), U.S. Army Engineer Waterways Experiment Station (WES), ATTN: ERDC-ITL-K, 3909 Halls Ferry Rd., Vicksburg, MS 39180-6199.]

Charnock, H., 1955: Wind stress on a water surface. *Quart. J. Roy. Meteor. Soc.,* **81,** 639–640.

Coleman, J. M., H. H. Roberts, and G. W. Stone, 1998: Mississippi River delta, an overview. *J. Coastal Res.,* **14,** 698–716.

Dawson, C., J. J. Westerink, J. C. Feyen, and D. Pothina, 2006: Continuous, discontinuous and coupled discontinuous–continuous Galerkin finite element methods for the shallow water equations. *Int. J. Numer. Methods Fluids,* **52,** 63–88.

Dietrich, J. C., R. L. Kolar, and J. J. Westerink, 2006: Refinements in continuous Galerkin wetting and drying algorithms. *Proc. Ninth Int. Conf. on Estuarine and Coastal Modeling,* Charleston, SC, ASCE, 637–656.

Federal Emergency Management Agency, 2006: Multi-hazard loss estimation methodology hurricane model. Dept. of Homeland Security Tech. Manual HAZUS MH MR3, 598 pp. [Available online at http://www.fema.gov/library/viewRecord.do?id=3034.]

Feyen, J. C., J. H. Atkinson, and J. J. Westerink, 2002: GWCE-based shallow water equation simulations of the Lake Pontchartrain–Lake Borgne tidal system. *Computational Methods in Water Resources,* Vol. II, S. M. Hassanizadeh et al., Eds., Developments in Water Science, Vol. 47, Elsevier, 1581–1588.

Flather, R. A., and K. P. Hubbert, 1990: Tide and surge models for shallow water—Morecambe Bay revisited. *Modeling Marine Systems,* Vol. I, A. M. Davies, Ed., CRC Press, 135–166.

Galland, J., N. Goutal, and J. Hervouet, 1991: A new numerical model for solving the shallow water equations. *Adv. Water Res.,* **14,** 138–148.

Garratt, J. R., 1977: Review of drag coefficients over oceans and continents. *Mon. Wea. Rev.,* **105,** 915–929.

Hagen, S. C., J. J. Westerink, and R. L. Kolar, 2000: Finite element grids based on a localized truncation error analysis. *Int. J. Numer. Methods Fluids,* **32,** 241–261.

——, ——, ——, and O. Horstmann, 2001: Two dimensional unstructured mesh generation for tidal models. *Int. J. Numer. Methods Fluids,* **35,** 669–686.

Holland, G., 1980: An analytic model of the wind and pressure profiles in hurricanes. *Mon. Wea. Rev.,* **108,** 1212–1218.

Hsu, S., 1988: *Coastal Meteorology*. Academic Press, 260 pp.

Kolar, R. L., W. G. Gray, J. J. Westerink, and R. A. Luettich, 1994a: Shallow water modeling in spherical coordinates: Equation formulation, numerical implementation and application. *J. Hydraul. Res.,* **32,** 3–24.

——, J. J. Westerink, M. E. Cantekin, and C. A. Blain, 1994b: Aspects of nonlinear simulations using shallow water models based on the wave continuity equation. *Comput. Fluids,* **23,** 523–538.

Leendertse, J. J., 1987: Aspects of SIMSYS2D: A system for two-dimensional flow computation. Rand Corporation Rep. R-3572-USGS, Santa Monica, CA, 80 pp.

Le Provost, C., F. Lyard, J. Molines, M. Genco, and F. Rabilloud, 1998: A hydrodynamic ocean tide model improved by assimilating a satellite altimeter-derived data set. *J. Geophys. Res.,* **103,** 5513–5529.

Lovelace, J. K., 1994: Storm-tide elevations produced by Hurricane Andrew along the Louisiana coast, August 25–27, 1992. U.S. Geological Survey Open File Rep. 94-371, Baton Rouge, LA, 45 pp.

Luettich, R. A., and J. J. Westerink, 1995: Continental shelf scale convergence studies with a barotropic model. *Quantitative Skill Assessment for Coastal Ocean Models,* D. R. Lynch and A. M. Davies, Eds., Coastal and Estuarine Studies Series, No. 47, Amer. Geophys. Union, 349–371.

——, and ——, 1999: Elemental wetting and drying in the ADCIRC hydrodynamic model: Upgrades and documentation for ADCIRC version 34.XX. Contractors Rep., U.S. Army Corps of Engineers, 8 pp. [Available from ERDC Vicksburg (WES), U.S. Army Engineer Waterways Experiment Station (WES), ATTN: ERDC-ITL-K, 3909 Halls Ferry Road, Vicksburg, MS 39180-6199.]

——, and ——, 2003: Combined discharge and radiation bound-

ary condition in the ADCIRC hydrodynamic model: Theory and documentation. Contractors' Rep., U.S. Army Corps of Engineers New Orleans District, 16 pp. [Available from U.S. Army Engineer Corps of Engineers, New Orleans, ATTN: CEMVN-IM-SM Library, P.O. Box 60267, New Orleans, LA 70160-0267.]

——, and ——, cited 2006a: ADCIRC: A parallel advanced circulation model for oceanic, coastal and estuarine waters; users manual for version 45.08. [Available online at http://adcirc.org/document/ADCIRC_title_page.html.]

——, and ——, cited 2006b: Formulation and numerical implementation of the 2D/3D ADCIRC finite element model, version 44.XX. [Available online at http://adcirc.org/adcirc_theory_2004_12_08.pdf.]

——, ——, and N. W. Scheffner, 1992: ADCIRC: An advanced three-dimensional circulation model for shelves, coasts and estuaries, Report 1: Theory and methodology of ADCIRC-2DDI and ADCIRC-3DL. Tech. Rep. DRP-92-6, U.S. Army Corps of Engineers, 137 pp. [Available from ERDC Vicksburg (WES), U.S. Army Engineer Waterways Experiment Station (WES), ATTN: ERDC-ITL-K, 3909 Halls Ferry Rd., Vicksburg, MS 39180-6199.]

Lynch, D. R., and W. G. Gray, 1979: A wave equation model for finite element tidal computations. *Comput. Fluids,* **7,** 207–228.

Mukai, A., J. J. Westerink, R. Luettich Jr., and D. Mark, 2002: Eastcoast 2001: A tidal constituent database for the western North Atlantic, Gulf of Mexico, and Caribbean Sea. Tech. Rep. ERDC/CHL TR-02-24, U.S. Army Corps of Engineers, 25 pp. [Available from ERDC Vicksburg (WES), U.S. Army Engineer Waterways Experiment Station (WES), ATTN: ERDC-ITL-K, 3909 Halls Ferry Rd., Vicksburg, MS 39180-6199.]

National Geophysical Data Center, 1998: *Geophysical Data System for Hydrographic Survey Data*. National Ocean Service Hydrographic Survey Data, National Geophysical Data Center, Boulder CO, 2 CD-ROMs.

——, cited 2006: ETOPO5 technical report. National Oceanic and Atmospheric Administration. [Available online at http://www.ngdc.noaa.gov/mgg/global/etopo5.HTML.]

National Wetlands Research Center, cited 2006: Land cover classification for the Louisiana GAP analysis. United States Geological Survey Tech. Rep. [Available online at http://sdms.cr.usgs.gov/gap/gap2.html.]

Powell, M., and S. Houston, 1996: Hurricane Andrew's landfall in south Florida. Part II: Surface wind fields and potential real-time applications. *Wea. Forecasting,* **11,** 329–349.

——, ——, and T. Reinhold, 1996: Hurricane Andrew's landfall in south Florida. Part I: Standardizing measurements for documentation of surface wind fields. *Wea. Forecasting,* **11,** 304–328.

——, ——, L. Amat, and N. Morrisseau-Leroy, 1998: The HRD real-time hurricane wind analysis system. *J. Wind Eng. Indust. Aerodyn.,* **77–78,** 53–64.

Rappaport, E., 2006: Preliminary report: Hurricane Andrew, 16–28 August 1992; updated 10 December 1993. National Oceanic and Atmospheric Administration/National Hurricane Center. [Available online at http://www.nhc.noaa.gov/1992andrew.html.]

Reid, R. O., and R. Whitaker, 1976: Wind-driven flow of water influenced by a canopy. *J. Waterways, Harbors, Coastal Eng. Div.,* **102,** 61–77.

Shinkle, K. D., and R. K. Dokka, 2004: Rates of vertical displacement at benchmarks in the Lower Mississippi Valley and the northern Gulf coast. NOAA Tech. Rep. NOS/NGS 50, 135 pp.

Simiu, E., and R. Scanlan, 1986: *Wind Effects on Structures*. Wiley Interscience, 604 pp.

Thompson, E. F., and V. J. Cardone, 1996: Practical modeling of hurricane surface wind fields. *J. Waterways Port, Coastal Eng.,* **122,** 195–205.

U.S. Army Engineer District New Orleans, 1965: Report on Hurricane Betsy, 8–11 September 1965 in the U.S. Army Engineer District, New Orleans. U.S. Army Corps of Engineers New Orleans District, Tech. Rep., 48 pp. [Available from U.S. Army Engineer Corps of Engineers, New Orleans, ATTN: CEMVN-IM-SM Library, P.O. Box 60267, New Orleans, LA 70160-0267.]

U.S. Geological Survey, cited 2006: National Elevation Dataset. EROS Data Center, Sioux Falls, SD. [Available online at http://ned.usgs.gov.]

Vogelmann, J. E., S. M. Howard, L. Yang, C. R. Larson, B. K. Wylie, and N. Van Driel, 2001: Completion of the 1990s National Land Cover Data Set for the conterminous United States from Landsat Thematic Mapper data and ancillary data sources. *Photogramm. Eng. Remote Sens.,* **67,** 650–652.

Westerink, J. J., R. A. Luettich, A. M. Baptista, N. W. Scheffner, and P. Farrar, 1992: Tide and storm surge predictions using a finite element model. *J. Hydraul. Eng.,* **118,** 1373–1390.

——, ——, and J. C. Muccino, 1994a: Modeling tides in the western North Atlantic using unstructured graded grids. *Tellus,* **46A,** 178–199.

——, ——, J. K. Wu, and R. L. Kolar, 1994b: The influence of normal flow boundary conditions on spurious modes in finite element solutions to the shallow water equations. *Int. J. Numer. Methods Fluids,* **18,** 1021–1060.

——, ——, and A. Militello, 2001: Leaky internal-barrier normal-flow boundaries in the ADCIRC Coastal Hydrodynamics Code. Coastal and Hydraulic Engineering Tech. Note IV-32, U.S. Army Corps of Engineers, 26 pp. [Available online at http://cirp.wes.army.mil/cirp/cetns/chetn-iv32.pdf or from ERDC Vicksburg (WES), U.S. Army Engineer Waterways Experiment Station (WES), ATTN: ERDC-ITL-K, 3909 Halls Ferry Rd., Vicksburg, MS 39180-6199.]